Molecular Therapy
Nucleic Acids
Original Article

Nimbolide-based nanomedicine inhibits breast cancer stem-like cells by epigenetic reprogramming of DNMTs-SFRP1-Wnt/β-catenin signaling axis

Priyanka Mohapatra,[1,2] Swati Madhulika,[1,2] Somalisa Behera,[1] Priya Singh,[1,2] Pratikshya Sa,[1,2] Punit Prasad,[1] Rajeeb Kumar Swain,[1] and Sanjeeb Kumar Sahoo[1]

[1]Institute of Life Sciences, Nalco Square, Bhubaneswar 751023, Odisha, India; [2]Regional Centre for Biotechnology, Faridabad 121001, Haryana, India

Triple-negative breast cancer (TNBC) harbors a high percentage of breast cancer stem-like cells (BCSCs) that significantly contribute to poor prognosis, metastasis, and relapse of the disease. Thus, targeting BCSCs could be a promising approach to combat TNBC. In this context, we investigated nimbolide (Nim), a limonoid triterpenoid that has potent anticancer properties, but poor pharmacokinetics and low bioavailability limit its therapeutic application. So, to enhance the therapeutic potential of Nim, Nim-encapsulated poly(lactic-co-glycolic acid) (PLGA) nanoparticles (Nim NPs) were formulated and the anticancer stem cell (CSC) effects evaluated *in vitro* and *in vivo*. *In vitro* studies suggested that Nim NPs significantly inhibited several inherent characteristics of BCSCs, such as stemness, self-renewability, chemoresistance, epithelial-to-mesenchymal transition (EMT), and migration in comparison to native Nim. Next, the mechanism behind the anti-CSC effect of Nim was explored. Mechanistically, we found that Nim epigenetically restores tumor suppressor gene secreted frizzled-related protein 1 (SFRP1) expression by downregulating DNA methyltransferases (DNMTs), leading to Wnt/β-catenin signaling inhibition. Further, *in vivo* results demonstrated that Nim NPs showed enhanced anti-tumor and anti-metastatic effects compared to native Nim in two preclinical models without any systemic toxicity. Overall, these findings provide proof of concept that Nim-based phytonanomedicine can inhibit BCSCs by epigenetic reprogramming of the DNMTs-SFRP1-Wnt/β-catenin signaling axis.

INTRODUCTION

Triple-negative breast cancer (TNBC) is an aggressive subtype of breast cancer, accounting for approximately 15%–20% of newly diagnosed cases with poor clinical outcomes.[1,2] Several studies have shown that drug resistance, metastasis, and tumor relapse are driven by a minor population of tumor-initiating cells called breast cancer stem-like cells (BCSCs), which exhibit properties such as quiescence, self-renewal, drug resistance, and epithelial-to-mesenchymal transition (EMT).[3–5] The current first-line treatment approach for TNBC patients consists of chemotherapeutics, mainly taxanes such as paclitaxel or docetaxel, which target rapidly proliferating cancer cells, whereas cancer stem cells (CSCs) remain unharmed due to quiescence and high expression of ABC transporters that leads to an increase in stemness, aldehyde dehydrogenase (ALDH)-positive BCSC population, and pro-inflammatory cytokines that drive tumor relapse and metastasis.[6–8] Therefore, targeting BCSCs is a promising approach for TNBC treatment.

Recently, phytochemicals have garnered significant attention as anticancer agents owing to their safety profile and efficacy in preclinical models due to their selectivity toward cancer cells and CSCs.[9,10] Nimbolide (Nim), a limonoid triterpene derived from the leaves of *Azadirachta indica*, has potent anticancer effects by regulating oxidative stress and inhibiting cell proliferation, EMT, metastasis, and angiogenesis in several cancers, including breast cancer.[11–13] Nim shows potential anticancer effects without exhibiting any side effects on normal cells,[14] making it an interesting candidate to be explored in clinical settings. However, its effect on BCSCs is still unknown; thus, we investigated its effect on BCSCs.

Aberrant epigenetic modifications of self-renewable pathways such as Wnt/β-catenin, Hedgehog, and Notch by DNA methylation or histone modification contribute to several inherent characteristics of BCSCs.[15,16] Wnt/β-catenin signaling is the master regulator of self-renewability, stemness, and migration in BCSCs.[17,18] Studies have reported that the tumor suppressor gene secreted frizzled-related protein 1 (SFRP1) negatively regulates Wnt/β-catenin signaling.[19] Epigenetic silencing of SFRP1 is mediated by promoter hypermethylation, resulting in a poor prognosis in breast cancer.[19–21] In consonance with this, human cancer database (Gene Expression Profiling Interactive Analysis [GEPIA2]) analysis revealed that SFRP1 expression is significantly lower in breast cancer tissues than in normal breast tissues. Thus, restoration of SFRP1 expression can lead to the downregulation of Wnt/β-catenin signaling in BCSCs. Hence, identifying a novel agent that can epigenetically reprogram

Received 11 February 2023; accepted 6 September 2023;
https://doi.org/10.1016/j.omtn.2023.102031.

Correspondence: Sanjeeb Kumar Sahoo, Cancer Nanomedicine Lab, Institute of Life Sciences, Nalco Square, Bhubaneswar 751023, Odisha, India.
E-mail: sanjeeb@ils.res.in

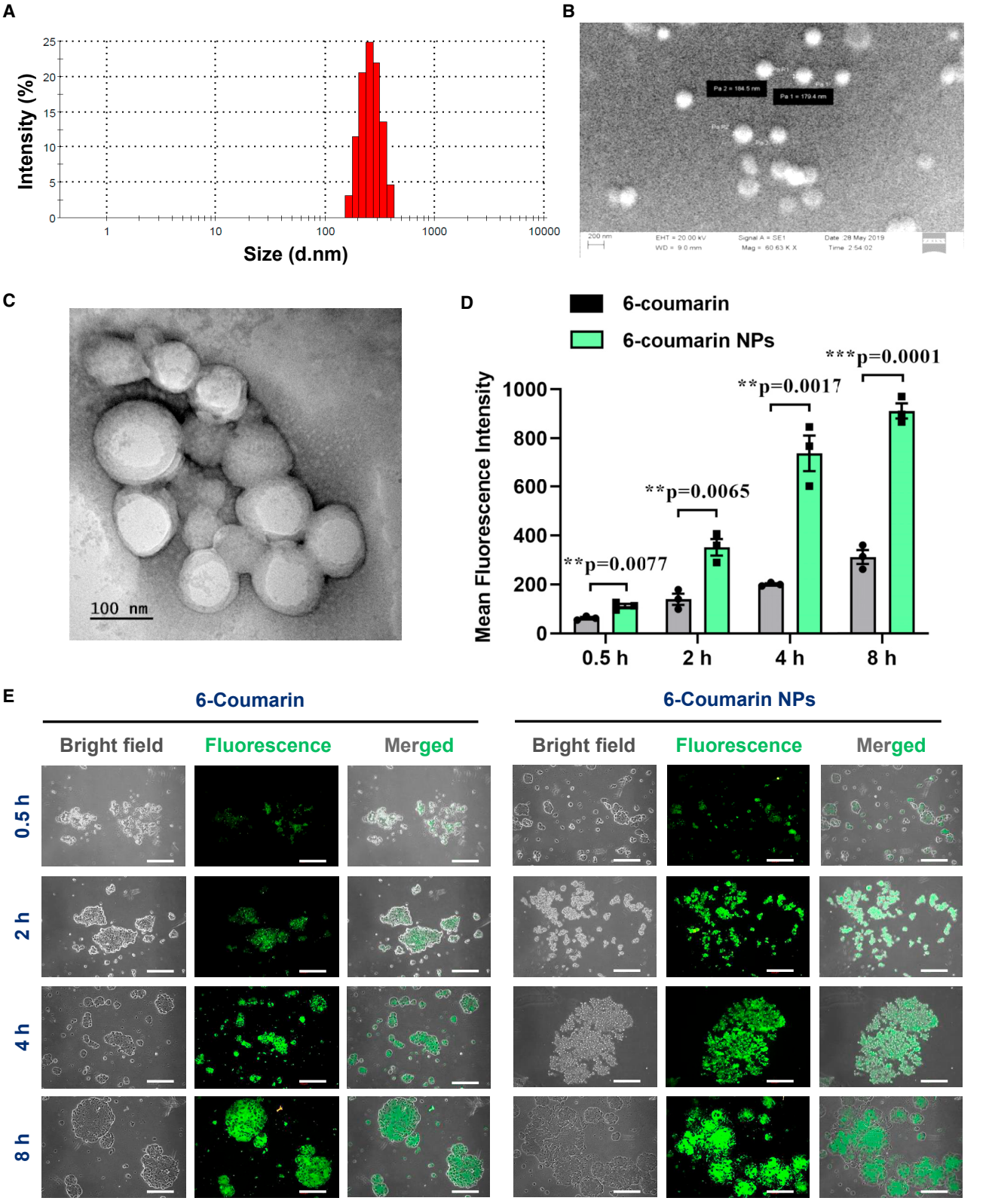

(legend on next page)

BCSCs has far-reaching potential in TNBC treatment. Studies have reported that phytochemicals such as genistein, EGCG, curcumin, sulforaphane, and resveratrol exhibit anticancer activity via epigenetic modulation of oncogenes and tumor suppressor genes through DNA methyltransferases (DNMTs) and histone deacetylases (HDACs) modifications.[22–24] Therefore, we investigated the effect of Nim on epigenetic modulation in BCSCs. However, poor pharmacokinetics and low bioavailability of Nim limit its therapeutic applications.

Nanotechnology is a cutting-edge technology that has paved the way for cancer drug delivery to enhance the inherent characteristics and improve the targeting ability of drugs through passive or active targeting.[25] Previously, we developed a forskolin-based nanomedicine that significantly improved the pharmacokinetics and targeting ability of forskolin, resulting in enhanced therapeutic efficacy of the phytochemical in a TNBC xenograft model.[5] In this study, we have formulated Nim-encapsulated poly(lactic-co-glycolic acid) (PLGA) nanoparticles (Nim NPs) and examined the anti-CSCs effects of Nim and Nim NPs in both *in vitro* (mammospheres) and *in vivo* (zebrafish and nude mice xenograft) models. *In vitro* results demonstrated that Nim NPs significantly reduced several inherent characteristics of BCSCs through epigenetic reprogramming of the DNMTs-SFRP1-Wnt/β-catenin signaling axis compared to native Nim. *In vivo* studies in two different preclinical models showed that Nim NPs enhanced anti-tumor and anti-metastatic efficacy compared to native Nim. Furthermore, it has been demonstrated through several assays on excised tumor tissues that epigenetic reprogramming results in the observed anti-tumor effects. Taken together, we conclude that Nim-based phytonanomedicine is a promising candidate for inhibiting BCSCs and can offer an efficient strategy for TNBC therapy.

RESULTS

Formulation, physicochemical characterization, and *in vitro* cellular uptake of formulated NPs

Nim-encapsulated PLGA NPs (Nim NPs) were formulated using polyvinyl alcohol (PVA) and D-a-tocopherol polyethylene glycol 1000 succinate (TPGS) as emulsifying agents by the single-emulsion solvent evaporation method (Figure S1A). The entrapment efficiency of Nim in Nim NPs was found to be ∼90%, as estimated by high-performance liquid chromatography (HPLC), with a loading efficiency of Nim of ∼9%. The average particle size of Nim NPs was found to be ∼250 nm, with a low polydispersity index (PDI) of ∼0.3, and zeta potential of approximately −23 mV, as determined by dynamic light scattering (Figures 1A and S1B). The scanning electron microscopy and atomic force microscopy (AFM) images showed uniform size with spherical morphology and smooth surface topology of the Nim NPs (Figures 1B and S1C). The transmission electron microscopy (TEM) images showed that the size of the Nim NPs was within the range of ∼130 nm (Figure 1C). The difference in particle size measured by zeta sizer and TEM may be due to hydrodynamic diameter and hydration of the surface-associated PVA probably contributing toward the hydrodynamic diameter of the NPs.[13,26] Fourier transform infrared (FTIR) spectra of void NPs, Nim, and Nim NPs are shown in Figure S1D. As there were no significant changes or loss of functional peaks between the spectra of Nim, void NPs, and Nim NPs, it can be concluded that there was no interaction between Nim and polymers in the formulation, so Nim has been encapsulated to the NPs efficiently. Previously, our group has formulated different drug-loaded PLGA NPs and has reported similar types of spectra to confirm the drug has been entrapped in NPs.[4,27] Further, we have studied the cellular uptake of NPs in MDA-MB-231-derived mammospheres using a fluorescent dye, 6-coumarin, incorporated in PLGA NPs. The dye is an excellent probe for NPs and offers a sensitive method to determine their intracellular uptake.[28] The quantitative intracellular uptake study showed that mammospheres treated with 6-coumarin NPs exhibited significantly higher fluorescence intensity in comparison to native 6-coumarin at different time points (Figure 1D). The above result was further corroborated by qualitative intracellular uptake of 6-coumarin NPs, and results revealed increased cellular uptake of 6-coumarin NPs as compared to native 6-coumarin in mammospheres at all the time points (Figure 1E).

Nim NPs induced cytotoxicity in BCSCs

The cytotoxic effects of Nim or Nim NPs were evaluated by 3-[4, 5-dimethylthiazol-2-yl]-2,5-diphenyltetrazolium bromide (MTT) assay. Results showed a higher cytotoxic effect of Nim NPs than that of native Nim in BCSCs in a concentration-dependent manner (Figures S2A and S2B). The half maximal inhibitory concentration (IC_{50}) values of native Nim and Nim NPs were 16.28 and 9.32 μM respectively 48 h post treatment, whereas they were 10.64 and 5.68 μM, respectively, 72 h post treatment (Table S1). The void NPs (PLGA NPs without Nim) used in this study were non-toxic. Further, the apoptotic potential of Nim or Nim NPs was evaluated, and results indicated that Nim NPs induced higher apoptosis compared to Nim in a concentration-dependent manner (Figures S2C and S2D). Cancer cells are known to elude apoptosis by downregulating pro-apoptotic proteins and constitutively activating anti-apoptotic proteins. To further validate the apoptotic potential, immunoblotting was performed, and results indicated that Nim NPs significantly upregulated pro-apoptotic proteins, whereas they downregulated anti-apoptotic proteins as compared to Nim, thereby delineating that Nim induced apoptosis in BCSCs (Figure S2E). Studies have reported that CSCs maintain low reactive oxygen species (ROS) and high expression of anti-oxidative enzymes through Nrf2 signaling, which regulates cellular redox homeostasis and facilitates resistance to therapies, self-renewability, and survival.[29–31] It has

Figure 1. Physicochemical characterization and cellular uptake of PLGA NPs

(A) Size of Nim NPs measured by DLS (n = 3). (B) Representative scanning electron microscope image of Nim NPs. (C) Representative TEM image of Nim NPs. (D) Quantitative cellular uptake study of 6-coumarin or 6-coumarin NPs (100 μg/mL) in BCSCs at different time intervals (0.5, 2, 4, and 8 h) by fluorescence spectrophotometer. Data represented as mean ± SEM (n = 3), unpaired two-tailed Student's t test. (E) Representative images of qualitative cellular uptake study of 6-coumarin or 6-coumarin NPs in BCSCs at different time intervals (0.5, 2, 4, and 8 h) by fluorescence microscopy. Scale bar, 200 μm.

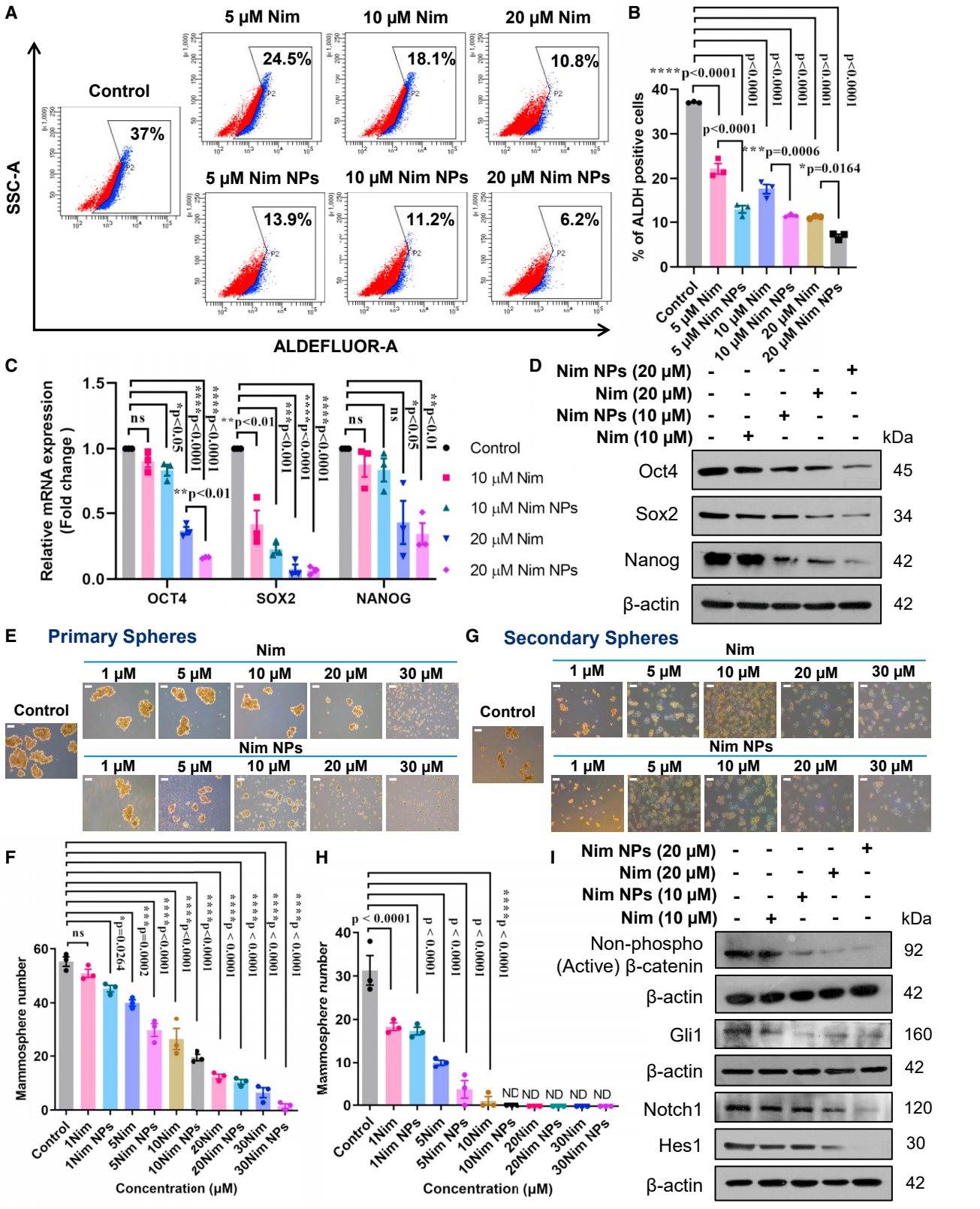

(legend on next page)

been documented that Nim induces ROS in osteosarcoma and pancreatic cancer cells *in vitro*.[14,32] In this context, we have checked intracellular ROS production in BCSCs by treating Nim or Nim NPs at different time points, and results demonstrate that Nim NPs induced higher ROS production as compared to Nim (Figure S3A). We have also checked the protein expression of Nrf2 and its downstream antioxidant enzymes superoxide dismutases (SOD), catalase, glutathione peroxidase (GPX), and glutathione reductase (GR) upon treatment with Nim or Nim NPs on BCSCs. Our results indicate that increased ROS production downregulates antioxidant protein expression in a concentration-dependent manner upon treatment with Nim or Nim NPs respectively (Figure S3B).

Nim NPs reduce stemness and self-renewability in BCSCs

High ALDH activity has been associated with stemness traits and is well documented as a putative CSCs marker, whereas the overexpression of stemness-specific transcription factors (Oct4, Sox2, and Nanog) may contribute to the maintenance of BCSCs.[5,33] In this context, we examined the effect of Nim or Nim NPs on ALDH-positive populations in BCSCs by ALDEFLUOR assay. Following treatment with Nim NPs, the ALDH-positive population was significantly reduced in comparison to native Nim (Figures 2A and 2B). Similarly, the stemness-associated markers Oct4, Sox2, and Nanog were significantly downregulated at both the mRNA and protein levels following treatment with Nim NPs compared to native Nim (Figures 2C and 2D). To further understand the effect of Nim and its nanoformulation on the self-renewal ability of BCSCs, we performed *in vitro* mammosphere formation assay. We evaluated the post-treatment sphere formation assay (Figure S4A), and the results indicated that the number and size of primary spheres treated with Nim or Nim NPs reduced in a concentration-dependent manner relative to control (Figures 2E, 2F, and S4B). Further, the study was carried out to understand whether these treated cells possess any residual stemness property after treatment. Hence, treated primary spheres were reseeded without further drug treatment for a week and exhibited reduced capacity of secondary sphere formation (Figures 2G, 2H, and S4C). It is worth mentioning that either Nim or Nim NPs inhibits the sphere formation, even at a low concentration of 5 μM, and Nim NPs (5 μM) showed better inhibitory effect than their native counterpart. The results indicate that BCSCs lose their self-renewal capacity after treatment. Thereafter, we performed preventive sphere formation assay (Figure S4D) and results showed that, upon treatment of Nim or Nim NPs, sphere-forming ability of MDA-MB-231 cells was hampered and further Nim NPs possessed a greater ability to prevent primary conversion of bulk tumor cells into BCSCs (Figures S4E–S4G). Further, to understand the self-renewability in BCSCs, we explored Wnt/β-catenin, Hedgehog, and Notch pathways that help to maintain the self-renewal characteristics. In this context, we have checked the above self-renewal pathways associated with protein expressions such as non-phospho (active) β-catenin (Wnt/β-catenin pathway), Gli1 (Hedgehog pathway), Hes1, and Notch1 (Notch pathway) after treatment with either native Nim or Nim NPs. Results show that Nim downregulated above protein expression in a concentration-dependent manner and protein expression is more downregulated in the case of Nim NPs than native Nim (Figure 2I).

Nim NPs reduce drug resistance, EMT, and metastasis in BCSCs

Drug resistance and metastasis are major causes of treatment failure and relapse in cancer patients.[34] In this regard, expression of drug efflux transporter (i.e., ABC transporter [ABCG2]) was analyzed in BCSCs following treatment with native Nim or Nim NPs for 48 h. Our results suggest that the expression of ABCG2 at both the mRNA and protein levels was considerably downregulated following treatment with Nim NPs compared to native Nim (Figures 3A and 3B). Studies suggest that EMT is a potential factor involved in CSC maintenance and metastasis.[35] Therefore, the expression of EMT master proteins were analyzed to determine whether Nim or Nim NPs inhibit CSCs migration by altering the EMT process. We evaluated the protein expression of the epithelial marker E-cadherin and mesenchymal markers N-cadherin, vimentin, Twist, and Snail. Results demonstrated that Nim or Nim NPs treatment significantly upregulated epithelial protein expression and downregulated mesenchymal protein expression, however, Nim NPs have shown a more prominent effect as compared to the native Nim (Figure 3C). By immunofluorescence assay, it was observed that E-cadherin expression was upregulated and vimentin expression was downregulated upon treatment with Nim or Nim NPs in a concentration-dependent manner (Figure 3D). Further, the effect of Nim or Nim NPs on CSCs migration was analyzed. Results indicated that chemokine receptor 4 (CXCR4; a prognostic metastatic breast cancer marker) expression was profoundly reduced in a concentration-dependent manner by Nim or Nim NPs both at mRNA and protein levels (Figures 3E and 3F). To study the effect of Nim on migration of CSCs, Transwell migration assay was performed. Results indicated that Nim NPs significantly reduced migration ability of mammospheres compared to Nim (Figures 3G and 3H).

Figure 2. Nim NPs reduce stemness and self-renewability in BCSCs

(A) Representative flow cytometry images of ALDH assay upon treatment with varying concentrations of Nim or Nim NPs. (B) Representative graph of ALDH assay. Data represented as mean ± SEM (n = 3). (C) Real-time PCR assay showing mRNA expression of stemness-associated genes, such as *OCT4*, *SOX2* and *NANOG* upon treatment with Nim or Nim NPs. Data represented as mean ± SEM (n = 3), one-way ANOVA with Tukey's multiple comparison test. (D) Immunoblotting analysis demonstrating protein expression of stemness markers Oct4, Sox2, and Nanog following treatment with Nim or Nim NPs. (E and G) Representative images of primary and secondary mammospheres post treatment with varying concentrations of either Nim or Nim NPs respectively. Scale bar, 50 μm. (F and H) Graphical representation of number of primary and secondary mammospheres after treatment with Nim or Nim NPs at different concentrations respectively. ND, not detected. Data represented as mean ± SEM (n = 3), one-way ANOVA with Tukey's multiple comparison test. (I) Immunoblotting analysis demonstrating protein expression of different self-renewal pathways such as Wnt/β-catenin signaling (non-phospho [Active] β-catenin), Hedgehog signaling (Gli1), and Notch signaling (Notch1 and Hes1) following treatment with Nim or Nim NPs.

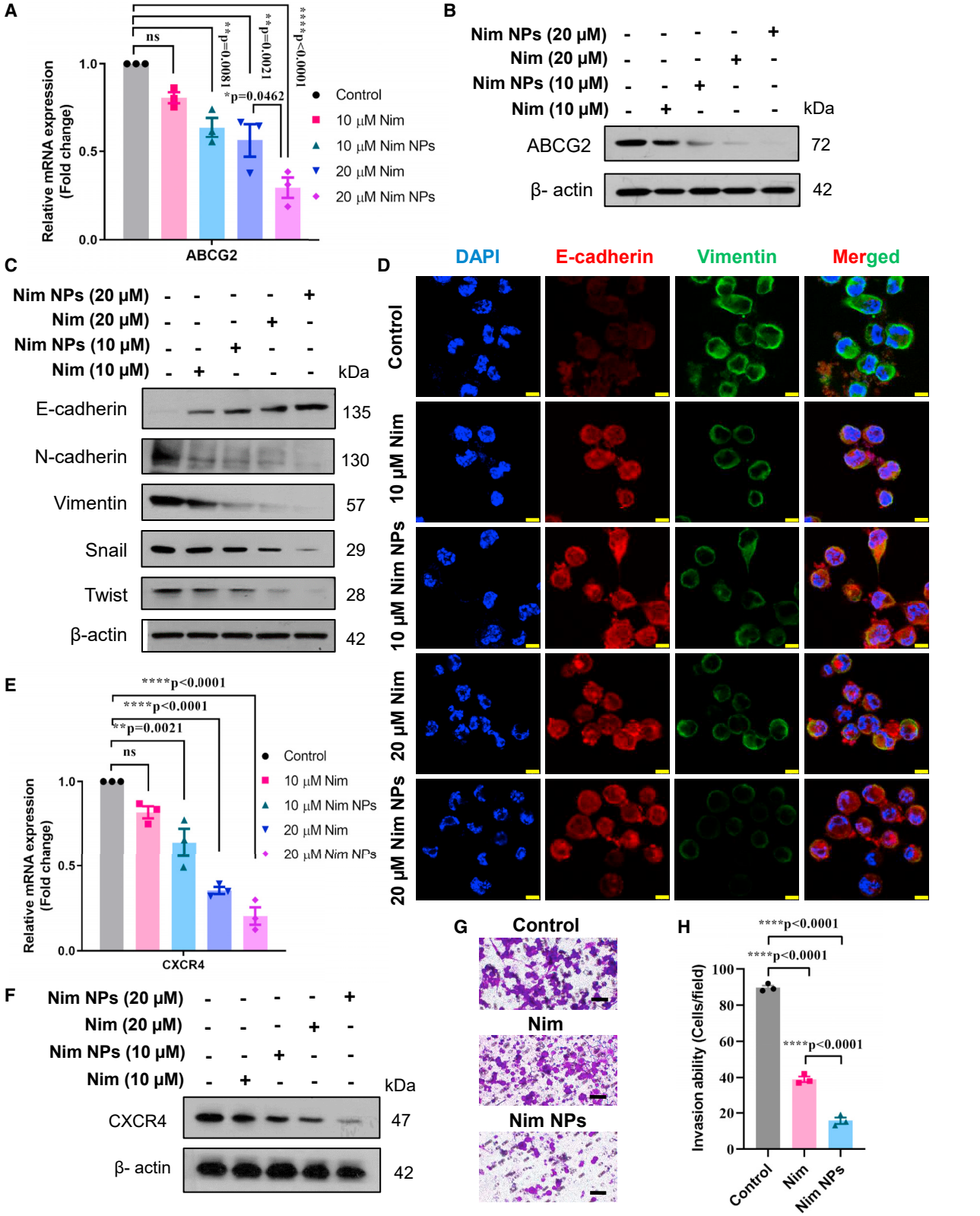

(legend on next page)

Nim inhibits DNMTs expression and promotes hypomethylation of *SFRP1* promoter, leading to inactivation of Wnt/β-catenin signaling in BCSCs

Wnt/β-catenin signaling plays an important role in the regulation of self-renewability and maintenance of the BCSCs.[36] The aberrant activation of Wnt/β-catenin signaling occurs through epigenetic silencing of tumor suppressor gene *SFRP1*.[20,37,38] Hence, we investigated the underlying epigenetic mechanism of SFRP1-Wnt/β-catenin signaling axis. The "Database: GEPIA2", data analysis portal revealed that *SFRP1* expression was significantly ($p < 0.05$) lower than *SFRP2/3/4/5* isoforms in breast cancer tissues compared to normal breast tissue (Figure 4A). Furthermore, gene expression and methylation status of *SFRP1* were analyzed by "Database: cBioportal", which revealed that the gene expression level of *SFRP1* was negatively correlated with the promoter methylation state in breast tumor cells (Figure 4B). β-Catenin (*CTNNB1*) gene is an important oncogene of Wnt/β-catenin signaling, and amplification of the *CTNNB1* gene is a possible mechanism of β-catenin overexpression in cancer, leading to carcinogenesis.[39] The pan-cancer analysis of RNA sequencing (RNA-seq) data by the "Database: TNMplot", demonstrated that *SFRP1* expression was significantly low in different tumor tissues compared to normal tissues, and *CTNNB1* expression was significantly higher in different tumor tissues than in normal tissues, particularly in breast cancer (Figures S5A and S5B). The pan-cancer "Database: TNMplot", heatmap analysis of RNA-seq data demonstrated that DNMTs (*DNMT1*, *DNMT3A*, *DNM3B*) expression was high, *SFRP1* expression was low, and *CTNNB1* expression was high in different tumor tissues compared to normal tissues, particularly in breast cancer (Figure S5C). Genome-wide transcriptomic data in breast invasive carcinoma also corroborated with the above analysis in tumor and metastatic tissues compared to normal breast tissue (Figure S5D). Thus, from the above analysis, we inferred that high DNMTs expression silences *SFRP1* gene, resulting in the upregulation of Wnt/β-catenin signaling. Thus, inhibition of DNMTs expression can lead to the restoration of SFRP1 expression, resulting in the downregulation of Wnt/β-catenin signaling. To prove our hypothesis, we successfully performed lentiviral-mediated short hairpin RNA (shRNA) knockdown of DNMTs (DNMT1, DNMT3A, and DNMT3B) (Figures S6A–S6C) and found SFRP1 expression was upregulated and, consequently, Wnt/β-catenin signaling was downregulated (Figures S6D–S6G).

We have analyzed the protein expression of DNMT isoforms (DNMT1, DNMT3A, and DNMT3B) in BCSCs and the results suggested that DNMT1 and DNMT3A expression was high compared to DNMT3B (Figures S7A–S7C). Hegde et al. have also reported similar results by analyzing DNMTs isoforms in different breast cancer subtypes (luminal, Her2 positive, and TNBC) compared to normal, where they found DNMT1 and DNMT3A expression to be high in TNBC in comparison to DNMT3B.[40] We therefore focused on DNMT1 and DNMT3A for detailed mechanism studies. Interestingly, in our study, we found that Nim inhibited the mRNA and protein expression of DNMTs in a concentration-dependent manner (Figures S8A and S8B). From the above results, we chose a lower concentration (5 μM) of Nim or Nim NPs, compared it with positive control 5-aza-2′-deoxycytidine/DAC (US Food and Drug Administration [FDA]-approved drug), and results revealed that both Nim and Nim NPs inhibited mRNA and protein expression of DNMTs (Figures 4C and 4D). Immunofluorescence results also corroborated the above analysis (Figures S8C–S8E). Further, we also found that expression of SFRP1 was upregulated upon treatment with Nim, Nim NPs, or DAC; however, Nim NPs and DAC showed better effect compared to native Nim (Figures 4E and 4F). The above results suggested that treatment of Nim or Nim NPs led to downregulation of DNMTs and upregulation of SFRP1 expression, indicating that Nim or Nim NPs possibly regulate SFRP1 through DNMTs. To further confirm that Nim inhibits SFRP1 hypermethylation by suppressing DNMT expression, cells were transiently overexpressed with DNMT1 and DNMT3A. The overexpression of DNMT1 and DNMT3A reduced the expression of SFRP1 and activated Wnt/β-catenin signaling upon Nim or Nim NPs treatment (Figures 4G and 4H). Furthermore, the overexpression of DNMTs also significantly prevented the inhibitory effects of Nim or Nim NPs on the cell viability of BCSCs (Figures S8F and S8G). Next, to understand the change in DNA methylation patterns of CpG islands before and after treatment with Nim or Nim NPs, we performed methylation-specific PCR (MSP) assay using different methylated and unmethylated specific primers from three different regions of SFRP1 CpG island (SCpGR1, SFRP1 CpG island region 1; SCpGR2, SFRP1 CpG island region 2; SCpGR3, SFRP1 CpG island region 3) (Figures S9A–S9C) (Table S4). The MSP results showed that treatment with Nim or Nim NPs significantly decreased the methylation ratio of SFRP1 (methylated/unmethylated) in BCSCs, where Nim NPs showed better inhibition compared to its native counterpart and also comparable to DAC (Figures 4I–4K and S10A–S10C). These global changes along with SFRP1 gene expression changes prompted us to investigate DNMTs' occupancies on different genomic loci in the SFRP1 gene

Figure 3. Nim NPs reduce drug resistance, EMT, and migration in BCSCs

(A) Real-time PCR assay showing mRNA expression of drug-resistance-associated gene- *ABCG2* upon treatment with Nim or Nim NPs. Data represented as mean ± SEM (n = 3), one-way ANOVA with Tukey's multiple comparison test. (B) Immunoblotting analysis demonstrating protein expression of drug resistance marker ABCG2 following treatment with Nim or Nim NPs. (C) Immunoblotting analysis demonstrating protein expression of epithelial marker such as E-cadherin and mesenchymal markers such as N-cadherin, vimentin, Twist, and Snail following treatment with Nim or Nim NPs. (D) Immunofluorescence images of epithelial marker (E-cadherin) and mesenchymal marker (vimentin) upon treatment with different concentrations of Nim or Nim NPs. Images taken at 63× objective. Scale bar, 7.5 μm. (E) Real-time PCR assay showing mRNA expression of a migration-associated gene *CXCR4* upon treatment with Nim or Nim NPs. Data represented as mean ± SEM (n = 3), one-way ANOVA with Tukey's multiple comparison test. (F) Immunoblotting analysis demonstrating protein expression of migration marker CXCR4 following treatment with Nim or Nim NPs. (G) Representative images of Transwell migration assay before and after treatment with Nim or Nim NPs (10 μM) in BCSCs. Images taken at 40× objective. Scale bar, 50 μm. (H) Graphical representation of the number of cells migrated by counting cells in five random fields using ImageJ software. Data represented as mean ± SEM, one-way ANOVA with Tukey's multiple comparison test.

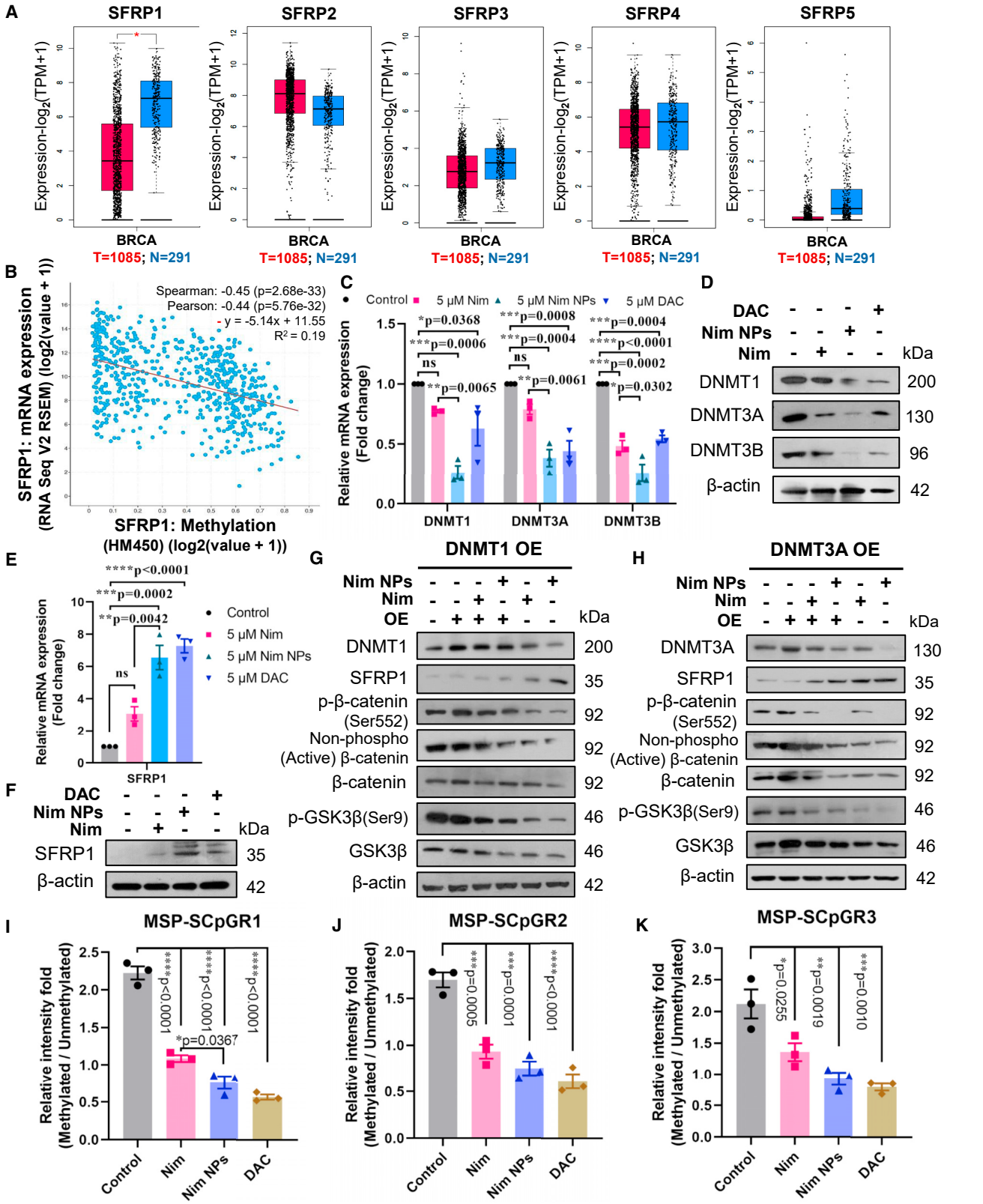

(legend on next page)

before and after treatment with Nim, Nim NPs, or DAC (Figures 5A and S11A). Chromatin immunoprecipitation (ChIP) followed by qPCR with DNMT1- and DNMT3A-specific antibodies showed their enrichment at the promoter and transcription start site (TSS) regions of *SFRP1* gene, whereas, upon treatment with Nim or Nim NPs, DNMT1 and DNMT3A occupancies significantly reduced. Moreover, the reduced enrichment of DNMTs with Nim NPs was very similar to DAC (Figures 5B–5I). We also used primers specific to a region upstream (non-CpG P10 −3.5 kb) and downstream (INT P9 18.5 kb) of TSS and showed that DNMTs do not get enriched in the absence of CpG islands (negative control), showing target specificity of the TSS primers used. Further, immunoblotting analysis demonstrated that protein expression of p-GSK3β (Ser9), non-p-active β-catenin, p-β-catenin (Ser552), cyclin D1, and c-myc downregulated upon Nim, Nim NPs, or DAC treatment in BCSCs (Figure 5J). Finally, these results indicate that Nim inhibits the ALDH-positive cell population by SFRP1-mediated Wnt/β-catenin signaling inhibition in BCSCs (Figures S8H–S8I).

In vivo pharmacokinetics and biodistribution of formulated NPs

We compared the pharmacokinetic profile of Nim NPs with native Nim after intravenous injection in BALB/c mice at a dose of 20 mg/kg body weight and estimated the concentration of Nim in blood serum at 0.5, 2, 6, 24, and 48 h post injection through HPLC. Results indicated that native Nim showed rapid clearance from blood and it was not detected in serum after 24 h of injection, whereas, in the case of Nim NPs, a high level of Nim was detected at initial time points, which gradually decreased but continued to be detected even after 48 h of injection (Figure S12A). Moreover, the half-life of Nim was significantly higher in Nim NPs besides improvement in all of the other pharmacokinetic parameters (Table S7). Thus, the above results indicated that nanoformulation improved the pharmacokinetic parameters of Nim in an *in vivo* system.

The *in vivo* biodistribution of IR 780-loaded PLGA NPs and native IR 780 dye was evaluated by intravenous administration into tumor-bearing nude mice through *in vivo* live imaging system (IVIS spectrum). As Nim has no intrinsic fluorescence to image *in vivo* through IVIS, IR 780 dye is used as a near-infrared probe that shows high and stable fluorescence intensity for *in vivo* imaging. Results indicated that fluorescence intensity of IR 780 NPs was significantly higher at tumor site compared to native IR 780 in a time-dependent manner post injection (Figure 6A). Further, qualitative and quantitative *ex vivo* results demonstrated that uptake of IR 780 NPs was almost three times higher than native IR 780 in the tumor, suggesting NPs taken up by tumor tissue through the enhanced permeability and retention (EPR) effect.[41] In contrast, IR 780 NP accumulation in major organs was low compared to native IR 780 (Figures 6B and 6C). Furthermore, 3D fluorescence imaging tomography (FLIT) fluorescence images of mice 24 h post injection were reconstructed with whole-body transillumination images using living image software 4.7.3, and the 3D region of interest (ROI) of the tumor was evaluated, indicating that IR 780 NPs accumulation at the tumor site was six times higher compared to native IR 780 (Figures 6D and 6E; Videos S1 and S2). The sensitivity of fluorescence detection can be improved through a calibration method called normalized transmission fluorescence (NTF) efficiency. Thus, the measured and simulated NTF efficiency profile of native IR 780 and IR 780 NPs were compared to check the reconstruction quality, providing good-quality 3D reconstruction (similar measured and simulated NTF efficiency) (Figures S13A and S13B). These biodistribution profiles indicated that the above nanoformulations have higher tumor accumulation ability through the EPR effect and remain longer at the tumor site.[42]

Therapeutic and anti-metastatic effect of Nim NPs in zebrafish xenograft

$ALDH^{high}$ BCSCs were labeled with Dil dye and injected into the perivitelline space of 2 days post-fertilization (dpf) transgenic zebrafish Tg(kdrl: EGFP) larvae. At 48 h post injection (hpi), embryos were treated with Nim or Nim NPs (1 or 2 μM) for 48 h to evaluate its anti-tumor and anti-metastatic efficacy (Figure 7A). Results indicated that, 48 h post treatment (hpt) with Nim or Nim NPs, there was significantly reduced tumor volume compared to the control group (Figures 7B and 7C). We assessed the cluster of metastatic cells in the tail of zebrafish before and after treatment. Results demonstrated that Nim NPs significantly decreased the number of metastatic cell clusters compared to native Nim or control group (Figures 7D and 7E). Taken together, these results indicate that Nim NPs reduced tumor volume and inhibited metastasis compared to native counterpart in zebrafish xenograft model. Further, we evaluated the expression of DNMT3A

Figure 4. Nim inhibits DNMTs expression and restores SFRP1 expression in BCSCs

(A) Boxplot showing the expression of SFRPs in breast cancer patients (GEPIA 2 database). The y axis log scale is represented as $\log_2$(TPM + 1), and the method for differential analysis is the one-way ANOVA, using disease state (tumor or normal) as the variable for calculating differential expression and statistical significance, with each dot representing a distinct tumor or normal sample. Red boxplot, tumor tissues (n = 1085); blue boxplot, normal tissues (n = 291). TPM, transcript per million. (B) The correlation between the gene expression level of SFRP1 and methylation rate of SFRP1 promoter from TCGA database, obtained by cBioportal Browser. (C) Real-time PCR assay showing mRNA expression of DNA methyltransferases (DNMTs) such as *DNMT1*, *DNMT3A*, and *DNMT3B* upon treatment with Nim, Nim NPs, and DAC. Data represented as mean ± SEM (n = 3), one-way ANOVA with Tukey's multiple comparison test. (D) Immunoblotting analysis demonstrating protein expression of DNMTs following treatment with Nim, Nim NPs, and DAC (5 μM) respectively in BCSCs. (E) Real-time PCR assay showing mRNA expression of *SFRP1* upon treatment with Nim, Nim NPs, and DAC. Data represented as mean ± SEM (n = 3), one-way ANOVA with Tukey's multiple comparison test. (F) Immunoblotting analysis demonstrating protein expression of SFRP1 following treatment with Nim, Nim NPs, and DAC. (G and H) pcDNA3/Myc-DNMT1 and pcDNA3/Myc-DNMT3A were transiently overexpressed and cells were treated with Nim or Nim NPs (5 μM) for 48 h and subjected to immunoblotting with indicated antibodies respectively. (I–K) Bar graph demonstrates quantification of methylation level at different regions of SFRP1 CpG island (SCpGR1, SCpGR2, and SCpGR3) in bisulfite-converted DNA with or without treatment with Nim, Nim NPs, or DAC (5 μM) measured by methylation-specific PCR (MSP) using methylation and unmethylation-specific primers. Data represented as mean ± SEM (n = 3), one-way ANOVA with Tukey's multiple comparison test. SCpGR1, SFRP1 CpG island region 1; SCpGR2, SFRP1 CpG island region 2; SCpGR3, SFRP1 CpG island region 3.

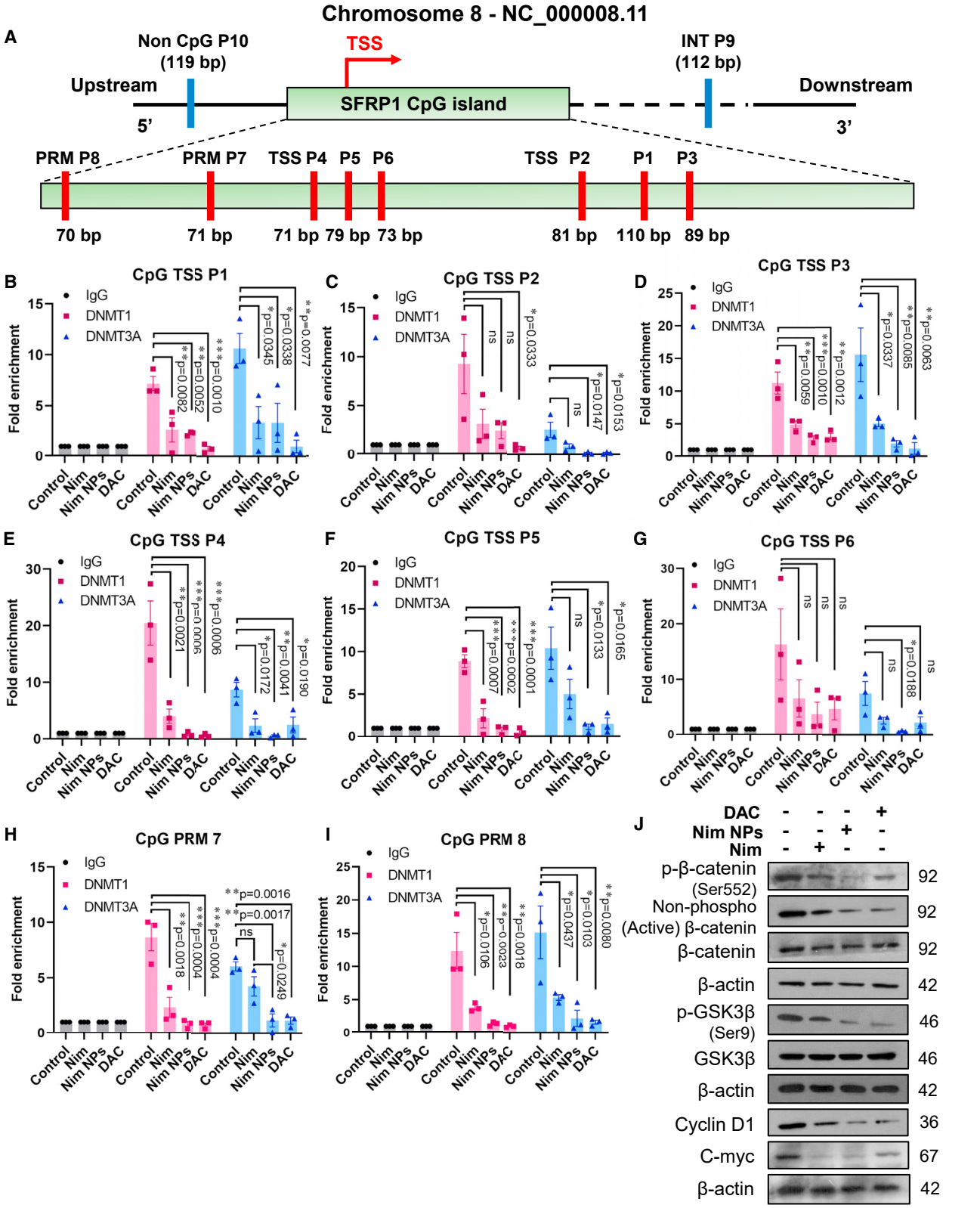

(legend on next page)

and β-catenin by immunofluorescence assay and results showed that Nim or Nim NPs significantly reduced DNMT3A and β-catenin expression in zebrafish tumors (Figures 7F, 7G, S14A, and S14B).

ALDH^{high} BCSCs induced tumorigenicity and therapeutic efficacy of Nim NPs in nude mice xenograft

We explored the tumorigenic ability of sorted ALDH^{high}/ALDH^{low} cells *in vivo* (Figure S15A). It was observed that ALDH^{high} cells generated tumors more aggressively than ALDH^{low} cells in Balb/c nude mice (Figures S15B–S15D). A similar result was reported by Mori et al., where they found injection of ALDH^{high} cells showed aggressive tumor as compared to ALDH^{low} cells.[43] The *in vivo* therapeutic efficacy of Nim or Nim NPs was accessed in orthotopic tumor-bearing nude mice as shown in Figure 8A. It has been observed that the tumor volume and tumor weight in the Nim- or Nim NP-treated groups were significantly reduced compared to control group throughout the study (Figures 8B–8D). The higher anti-tumor effect was observed in Nim NPs (20 mg/kg); more importantly, Nim NPs (10 mg/kg) showed better anti-tumor effect than Nim (20 mg/kg). Moreover, we found that there was no change in body weight, suggesting that the above injected nanoformulation was non-toxic (Figure S16A). In addition, no mice in any group died during the experiment or showed damage to their major organs, as depicted by hematoxylin-eosin (H&E) staining performed at the end of the experiment, indicating that the above dose is non-toxic (Figure S16B). Further, to evaluate the anti-metastatic properties of Nim and Nim NPs, we studied the metastatic nodes in different organs. It is well documented that breast cancer spreads from its primary site to secondary sites of the body, but mainly metastasizes to the bone, lungs, and liver.[44] In our study, we found that the metastatic nodules decreased in the major organs such as liver, lungs, and spleen in Nim or Nim NP-treated groups compared to control group, whereas no metastatic nodes were found in the Nim NPs (20 mg/kg) treatment group (Figure 8E). Next, we evaluated protein expression of the DNMTs-SFRP1-Wnt/β-catenin signaling axis in excised tumor tissue of different treatment groups. Nim or Nim NPs treatment significantly reduced the protein expression of DNMTs and induced SFRP1 expression, which led to downregulation of Wnt/β-catenin signaling-associated proteins in tumors of mice xenograft. Further, we found that stemness proteins, such as Oct4, Sox2, and Nanog, were also downregulated upon treatment in mice tumor tissue as compared to control (Figure 8F). Immunohistochemistry (IHC) results demonstrated that the numbers of Ki67-positive cells in tumor tissue were significantly reduced in Nim or Nim NP-treated groups compared to the control group (Figures 8G and 8H), suggesting that proliferation was inhibited. Furthermore, IHC results revealed that the expression of β-catenin in tumor tissues from Nim or Nim NP-treated groups was lower as compared to the control group (Figures 8I and 8J). Taken together, these results demonstrated that Nim NPs markedly inhibited tumor growth and stemness and also suggested that Nim has a potent anti-tumor effect in the breast cancer mice xenograft model.

DISCUSSION

Accumulating evidence has implicated BCSCs as a major cause of chemoresistance, metastasis, and relapse in TNBC. BCSCs exhibit resistance to current treatment regimens due to several intrinsic characteristics, including high expression of ABC transporters, low ROS level, increased ALDH activity, EMT, self-renewability, and differentiation.[45,46] Self-renewal ability is an important characteristic of BCSCs that helps to reinitiate tumors, leading to relapse.[47] Studies suggest that, among all self-renewal pathways, Wnt/β-catenin signaling is the key regulator of self-renewability, chemoresistance, and migration in BCSCs.[36,47,48] However, the Wnt/β-catenin pathway is aberrantly activated by epigenetic modifications that contribute to the initiation and progression of various human cancers, including breast cancer.[16] SFRP1, a tumor suppressor gene, acts as an antagonist to Wnt/β-catenin signaling, and further evidence suggested that epigenetic silencing of SFRP1 is linked with the abnormal activation of Wnt/β-catenin signaling.[38] From The Cancer Genome Atlas (TCGA) database cBioportal, GEPIA2, and TNMplot analysis, we inferred that SFRP1 expression is significantly lower in breast cancer tissues than in normal breast tissues due to frequent hypermethylation leading to poor prognosis. Thus, targeting BCSCs by epigenetic reprogramming of the SFRP1-Wnt/β-catenin signaling axis may be an effective approach for breast cancer management. Recently, phytochemicals have gained immense attention as potent anti-oxidative and anticancer agents because of their safety profile and privileged scaffold, which allows the inhibition of multiple targets within a common oncogenic pathway or many oncogenic pathways simultaneously to target cancer cells and CSCs.[9,10] Nim is a phytochemical that exhibits potent anticancer effects in a variety of solid tumors, including breast cancer, but its effect on BCSCs remains unknown. Hence, we explored the anti-CSC effect and mechanism of action of Nim in BCSCs. However, Nim is associated with low bioavailability and poor pharmacokinetics, which limits its therapeutic application.[49] In this context, we employed a nanomedicinal approach to enhance the therapeutic index of Nim, as nanomedicine has proved its potential in increasing pharmacokinetics and bioavailability of the drug by delivering the drug at the tumor site through the EPR effect.[50] PLGA is an effective polymer used in nanomedicine because of

Figure 5. Nim inhibits SFRP1 promoter hypermethylation and consequently downregulates Wnt/β-catenin signaling in BCSCs

(A) Schematic representation of SFRP1 gene locus and regions analyzed before and after Nim or Nim NP treatment. The solid box (green) represents SFRP1 CpG island, lines (red) represent the regions evaluated to estimate methylation status before and after treatment of Nim or Nim NPs compared to the positive control DAC, and lines (blue) represent negative controls selected from upstream and downstream of non-CpG region. (B–I) Chromatin immunoprecipitation (ChIP)-qPCR represents DNMT (DNMT1 and DNMT3A) enrichment in different CpG island regions such as transcription start site (TSS 1–6) and promoter (PRM 7–8) of the SFRP1 gene before and after treatment with Nim, Nim NPs, and DAC (5 μM) respectively in BCSCs. IgG pull-down was used as the control. Data represented as mean ± SEM (n = 3), one-way ANOVA with Tukey's multiple comparison test. (J) Immunoblotting analysis demonstrating protein expression of Wnt/β-catenin signaling associated markers following treatment with Nim, Nim NPs, and DAC (5 μM), respectively, in BCSCs.

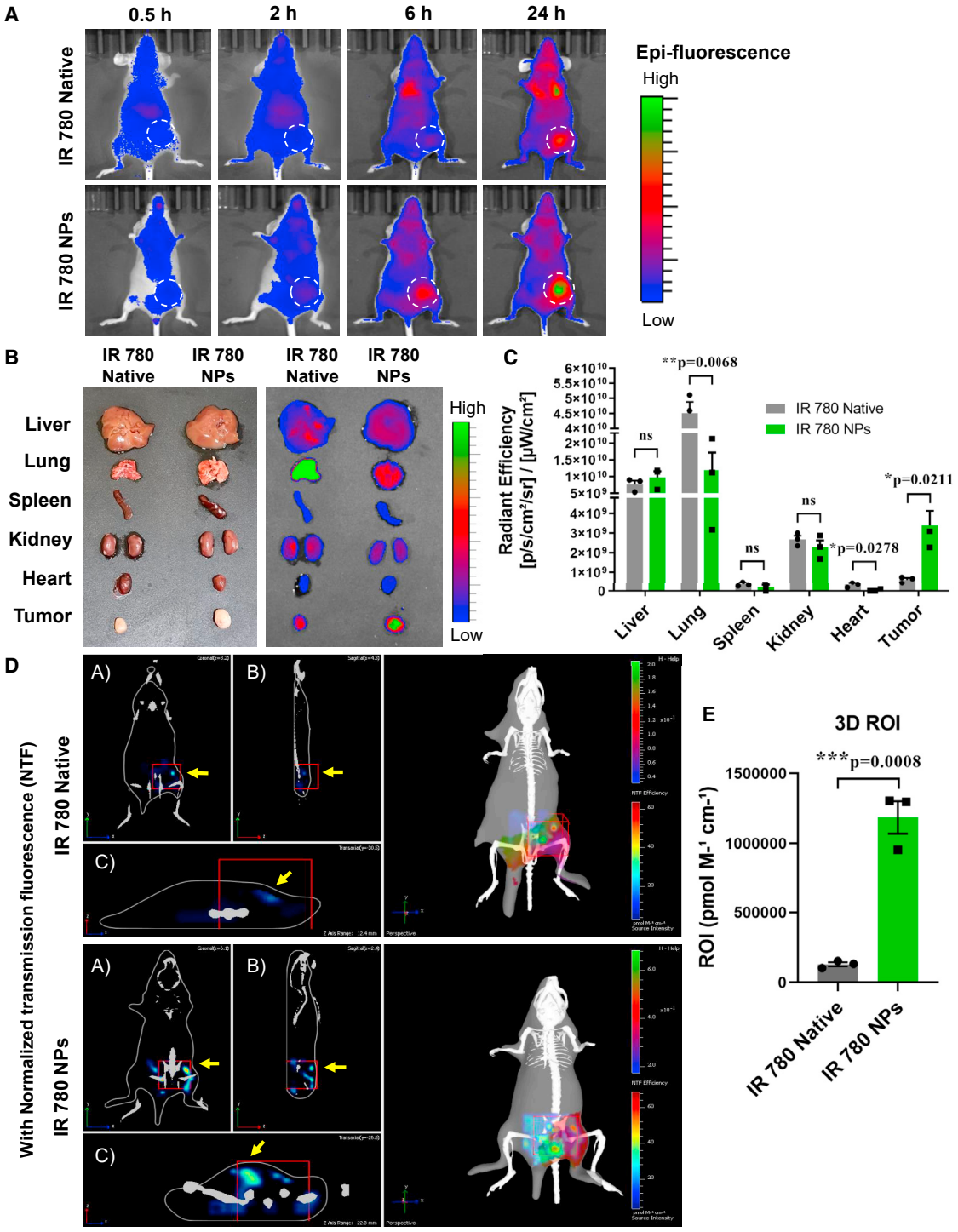

Figure 6. *In vivo* biodistribution of IR 780 native and IR 780 NPs in nude mice xenograft

For biodistribution studies, IR 780 dye-loaded PLGA NPs were formulated, 0.5 mg/kg body weight was injected intravenously into the orthotopic tumor-bearing mice, and live animal imaging was performed through IVIS Spectrum. (A) Representative 2D images by IVIS live imaging of nude mice after administration of IR 780 native and IR 780 NPs at different time points (0.5, 2, 6, and 24 h). (B) Representative *ex vivo* images of organs (liver, lung, spleen, kidney, and heart) and excised tumors from mice after 24 h of injection. (C) Graphical representation demonstrating fluorescence intensity measurement of IR 780 signal obtained from the isolated organs and tumor. Data represented as mean ± SEM (n = 3), unpaired two-tailed Student's t test. (D) 3D FLIT reconstruction of fluorescence sources in mice 24 h post injection reconstructed with whole-body transillumination images by living image software 4.7.3. Mouse tomography is represented in different directions: (A) coronal, (B) sagittal, and (C) transaxial. (E) Graphical representation showing 3D region of interest (ROI) measurement of the tumor. Data represented as mean ± SEM (n = 3), unpaired two-tailed Student's t test.

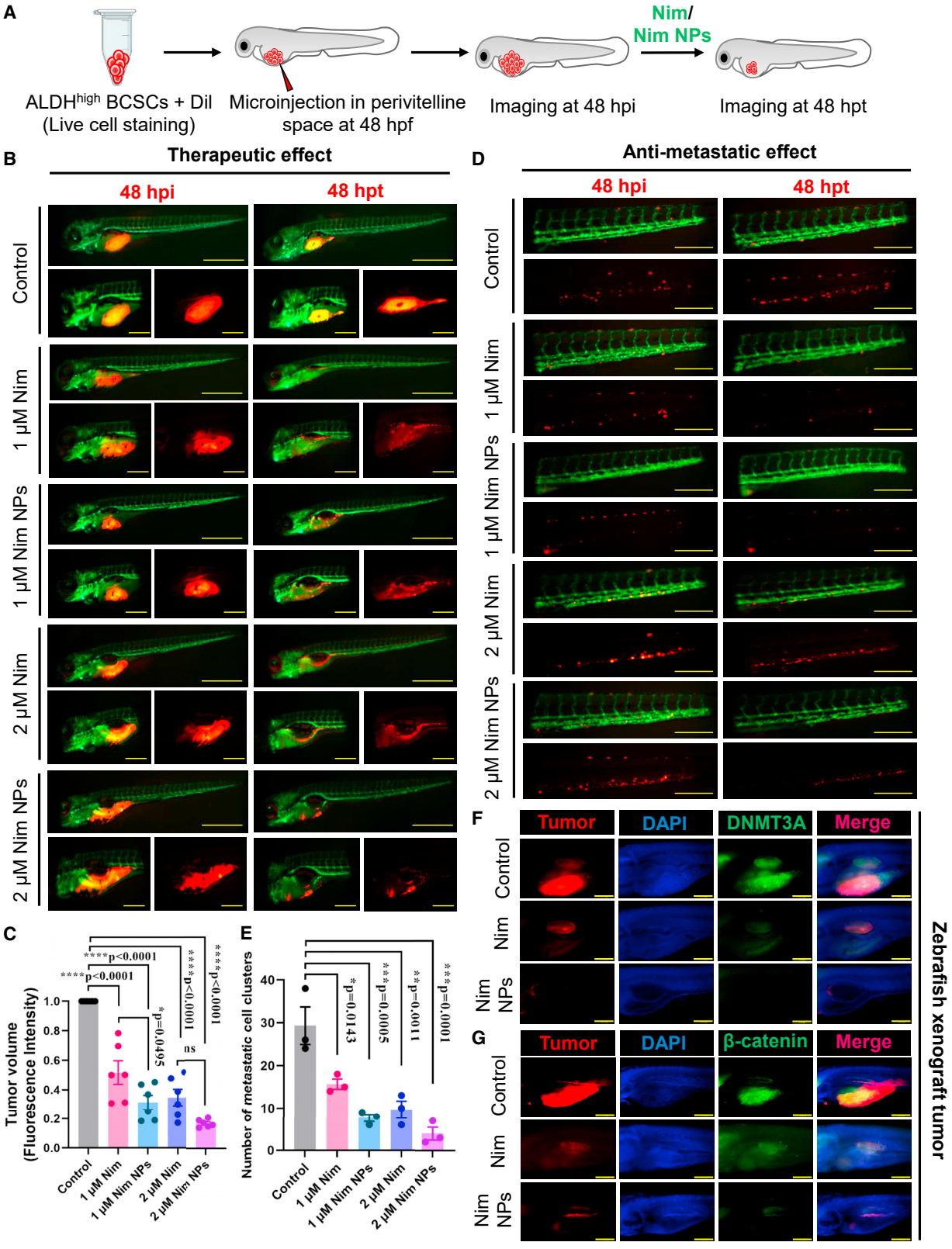

(legend on next page)

its controlled drug release profile and excellent biocompatible and biodegradable properties.[42] Thus, in this study, we formulated Nim-encapsulated PLGA NPs as it can mitigate the intrinsic properties of Nim, and, further, we investigated the therapeutic efficacy of Nim NPs compared to native Nim in *in vitro* and *in vivo* models.

Enhanced cellular internalization of drug-loaded NPs is a prerequisite for an efficient cancer-therapeutic approach.[51] In our study, PLGA nanoformulations containing 6-coumarin as a fluorescent marker exhibited significantly higher intracellular uptake efficiency than its native counterpart in BCSCs. Nim NPs showed higher *in vitro* cytotoxicity as compared to native Nim in BCSCs. It has been reported that CSCs maintain low ROS levels and high expression of anti-oxidative enzymes through Nrf2 signaling, which regulates cellular redox homeostasis and facilitates chemoresistance and survival.[52–55] In this context, in our study, Nim or Nim NPs elevated ROS levels in BCSCs by downregulating Nrf2 and various antioxidant proteins. Furthermore, the reduced expression of stemness and ALDH-positive cell populations indicated that the cells lost their stemness characteristics significantly following treatment with Nim NPs compared to Nim in BCSCs. Next, to understand the effect of Nim or Nim NPs on the self-renewal ability of BCSCs, sphere formation assay was performed, which is a well-established *in vitro* method for assessing the self-renewal properties of CSCs.[5] We observed that low concentrations of Nim or Nim NPs reduced the sphere-forming ability of primary and secondary mammospheres, with Nim NPs showing better inhibitory effect as compared to native Nim. Further, preventive sphere formation assay showed that Nim NPs significantly inhibit the sphere-forming ability of adherent cells to mammospheres, suggesting that Nim NPs inhibited self-renewal ability of BCSCs more efficiently compared to Nim. Further, we examined the effect of Nim or Nim NPs on the protein expression of the self-renewal pathways such as Wnt/β-catenin, Hedgehog, and Notch signaling and found that Nim NPs showed profound inhibitory effects compared to Nim. Accumulating evidence suggests that BCSCs are responsible for drug resistance through the overexpression of efflux transporters.[3] In our study, we observed that Nim NPs significantly reduced the expression of ABCG2, which is a marker for drug resistance in BCSCs compared to Nim. Recent evidence suggests that CSCs play a key role in the metastasis and relapse of tumors by undergoing EMT.[56,57] In this milieu, we have demonstrated that either native Nim or Nim NPs inhibited EMT-associated protein expression and the migration ability of BCSCs; however, Nim NPs inhibit better than native Nim. The above *in vitro* studies demonstrated that Nim and its nanoformulation significantly inhibited several inherent characteristics of BCSCs.

Next, we investigated the detailed mechanism of action responsible for the multimodal effect of Nim on BCSCs. As discussed above, Wnt/β-catenin signaling is the key regulator in BCSCs and epigenetic silencing of SFRP1 contributes to abnormal activation of this pathway.[17,19,20] Thus, our focus was to understand the effect of Nim on the epigenetic reprogramming of the SFRP1-Wnt/β-catenin signaling axis. As proof of the hypothesis, we observed in our study that shRNA-mediated knockdown of DNMTs induced SFRP1 restoration that led to downregulation of Wnt/β-catenin signaling. We evaluated the expression levels of different DNMTs isoforms in BCSCs and found that DNMT1 and DNMT3A expression was high as compared to DNMT3B, and a similar result was also reported in TNBC patients.[40] We therefore mainly focused our study on DNMT1 and DNMT3A. Further, we tried to understand the effect of Nim on DNMTs as it is responsible for SFRP1 hypermethylation and found that, at a lower concentration of Nim, Nim NPs and 5-aza-2′-deoxycytidine/DAC (positive control) showed downregulation of DNMT expression and upregulation of SFRP1 expression. ChIP gave direct evidence that DNMT recruitment is compromised with Nim or Nim NPs treatment resulting in hypomethylation of SFRP1 promoter and its upregulation. In a similar line, a study by Xie et al. showed that treatment of 5-aza-2′-deoxycytidine increases the expression of SFRP1 by reducing the enrichment of DNMTs at SFRP1 promoter in HBV-related hepatocellular carcinoma.[58] Further, treatment with Nim or Nim NPs after overexpression of DNMTs resulted in reversing the effects of Nim or Nim NPs on SFRP1 and β-catenin, suggesting that indeed Nim shows anti-CSCs effects through DNMTs-SFRP1-Wnt/β-catenin signaling axis. These findings suggest that reduced enrichment of DNMTs and concomitant upregulation of SFRP1 is due to reduced levels of DNMT proteins, suggesting that the recruitment defect could be merely a result of reduced gene expression.

During the past decade, Nim has shown promising anticancer efficacy, but its poor pharmacokinetics and low bioavailability in animal models diminish its therapeutic effect.[59] In this context, we have formulated Nim-loaded PLGA NPs that have shown improved pharmacokinetic parameters and tumor-targeting ability upon systemic administration in mice. The *in vivo* biodistribution profiles of the NPs showed better tumor accumulation through the EPR effect and significantly higher retention at the tumor site for a longer period (i.e., more than 24 h

Figure 7. *In vivo* anti-tumor and anti-metastatic efficacy of Nim NPs in zebrafish xenograft

(A) Experimental layout for therapeutic and anti-metastatic studies in tumor-bearing zebrafish xenograft model. (B) $ALDH^{high}$ BCSCs were stained with DiI and transplanted into transgenic zebrafish embryos (Tg(kdrl: EGFP)) at the perivitelline space 48 h post fertilization (hpf) under the microscope. Further, 48 h post-injection (hpi) zebrafish were imaged by stereomicroscope and then treated with Nim or Nim NPs (1 or 2 μM). Zebrafish were again imaged 48 h post treatment (hpt) to estimate the tumor reduction after treatment (n = 6). Whole-fish images were taken at 25× objective. Scale bar, 1.1 mm. Zoomed images of the head were taken at 75× objective. Scale bar, 368.4 μm. (C) Graphical representation showing reduction of tumor volume after treatment with Nim NPs compared to Nim. Data represented as mean ± SEM (n = 6), one-way ANOVA with Tukey's multiple comparison test. (D) Effect on tumor cell metastasis was detected upon treatment with Nim or Nim NPs (1 or 2 μM) using a stereomicroscope at 48 hpt in zebrafish xenograft. Zoomed images of the tail were taken at 75× objective. Scale bar, 368.4 μm. (E) Graphical representation of metastatic cell clusters before and after treatment with Nim or Nim NPs. Data represented as mean ± SEM (n = 3), one-way ANOVA with Tukey's multiple comparison test. (F and G) Representative immunofluorescence images by stereomicroscope shows the expression of DNMT3A and β-catenin before and after treatment of Nim or Nim NPs (2 μM) in zebrafish xenograft. Images were taken at 126× objective. Scale bar, 172.1 μm.

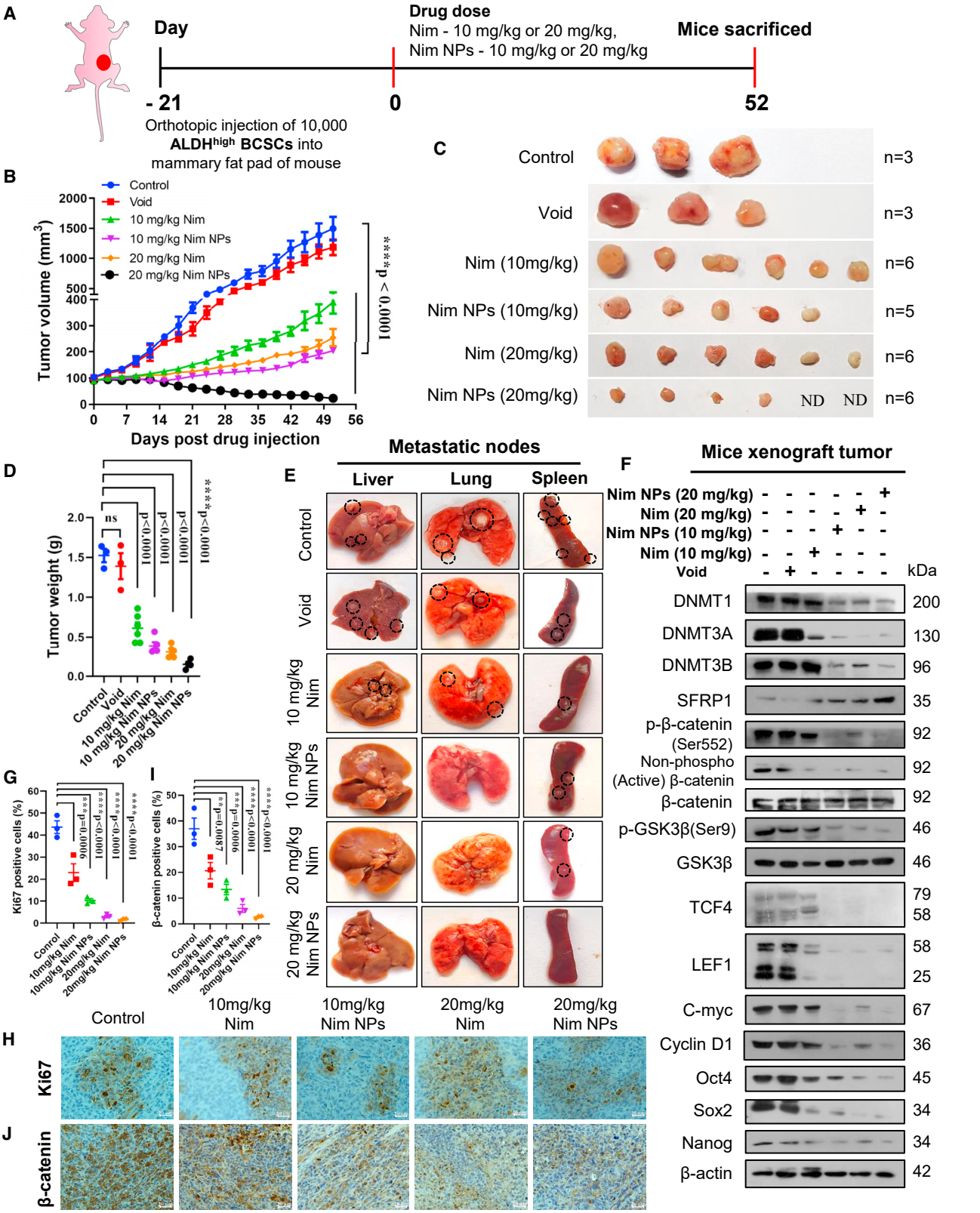

(legend on next page)

post treatment) than native counterpart. Further, we have validated the therapeutic and anti-metastatic effects of Nim or Nim NPs in zebrafish and mice xenograft models. Recently, zebrafish have gained much attention as an ideal model for cancer research because of cost-effective maintenance, dynamic visualization of tumor growth, and rapid validation of anticancer or anti-metastatic drugs *in vivo*.[60] In our study, we have demonstrated that a lower dose of Nim or Nim NPs significantly reduced tumor size in perivitelline space as well as number of metastatic cell clusters in the tail of zebrafish xenografts, whereas Nim NPs showed better anti-tumor and anti-metastatic potential as compared to Nim. In consonance with the *in vitro* results, we observed that DNMT3A and β-catenin were significantly downregulated in tumor after treatment with Nim or Nim NPs in zebrafish embryos. Next, the anti-tumor efficacy of Nim or Nim NPs was investigated in another preclinical model, orthotopic mouse xenograft, which is an excellent model for therapeutic and metastatic studies as it resembles human tumorigenesis.[61] *In vivo* results in mice demonstrated that administration of a single dose of Nim or Nim NPs (10 mg/kg or 20 mg/kg) significantly reduced tumor volume; however, Nim NPs (10 mg/kg) showed better anti-tumor efficacy than native Nim (20 mg/kg). Interestingly, we found that 20 mg/kg Nim NPs drastically reduced the tumor burden after 7 weeks of treatment compared to the other treatment groups. Here, it is noteworthy to mention that the administered doses of formulated nanomedicine and its native counterpart showed no systemic toxicity (as no major change in body weight and no damage in major organs) in mice. Breast cancer spreads from its primary site (breast) to secondary sites in the body, such as bone, lungs, liver, brain, lymph nodes, and spleen.[62] It has been reported that, in the orthotopic mice xenograft model, micrometastasis starts after 1 week and large micrometastatic nodules from 2 to 5 weeks after cancer cell implantation.[63] As our experimental setup was for a longer period of time, we observed metastatic nodes in lungs, liver, and spleen of mice xenograft. However, in our study, we found that the number of metastatic nodes decreased in different treatment groups, whereas Nim NPs (20 mg/kg) as a dose showed better anti-metastatic effect in the mouse model. We made an interesting observation that, apart from inhibiting tumor growth, Nim NPs significantly reduced metastasis as well. We next validated the mechanism of action of Nim in different tumors of mice xenograft and found downregulation of DNMTs, upregulation of SFRP1, and reduced active β-catenin and its downstream proteins upon Nim or Nim NPs treatment. From the above *in vitro* and *in vivo* study, we conclude that Nim NPs showed better inhibitory effects in BCSCs by epigenetic reprogramming of DNMTs-SFRP1-Wnt/β-catenin signaling axis.

In conclusion, our research demonstrates that Nim inhibits BCSCs by epigenetic reprogramming of the DNMTs-SFRP1-Wnt/β-catenin signaling axis that plays an important role in maintaining several intrinsic characteristics of BCSCs *in vitro* and *in vivo*. Our results suggested that Nim-based nanomedicine shows better therapeutic and anti-metastatic effects in preclinical models due to higher cellular uptake and passive tumor accumulation through the EPR effect. Hence, this formulated Nim-loaded phytonanomedicine has the potential to be explored in the clinical setting to achieve complete tumor eradication in TNBC patients.

MATERIALS AND METHODS

Reagents

Nimbolide was purchased from Asthagiri Herbal Research Foundation (AHRF) (Tamil Nadu, India). 5-Aza-2′-deoxycytidine was purchased from Sigma-Aldrich (catalog # A3656). PLGA (copolymer ratio 50:50, I.V. = 0.55–0.75) was purchased from Birmingham Polymers (Birmingham, AL). StemPro Accutase was procured from Gibco Laboratories (MD, USA). Annexin V/PE apoptosis detection kit was purchased from BD Biosciences (CA, USA). The 3-[4, 5-dimethylthiazol-2-yl]-2,5-diphenyltetrazolium bromide (MTT), 2′,7′-dichlorofluorescein diacetate (DCFDA), propidium iodide, RNase, insulin, bovine serum albumin (BSA), and Triton X-100 were procured from Sigma-Aldrich, (St. Louis, USA).

Preparation of drug-loaded PLGA NPs

Nim-loaded PLGA NPs were prepared by oil-in-water (O/W) single-emulsion solvent evaporation method (loading 10% w/w with respect to the weight of the polymer). Briefly, 2% PVA (average molecular weight [MW] 31,000–50,000; Sigma-Aldrich, St. Louis, USA) and 0.1% D-a-tocopherol polyethylene glycol 1000 succinate (TPGS) (Sigma-Aldrich, St. Louis, USA) was dissolved in 12 mL of H_2O w/v with stirring followed by dissolving 100 mg of PLGA polymer in 3 mL of organic solvent (chloroform) (HPLC grade; Merck, India). Then 10 mg of Nim was added to the polymeric solution and vortexed until it dissolved to form a primary emulsion loading 10% (w/w) of the polymer. The emulsion was further emulsified in an aqueous phase (PVA and TPGS dissolved in H_2O w/v) drop by drop while vortexing to form an oil-in-water emulsion. The above solution was sonicated using a sonicator (VC 505, Vibracell Sonics, USA) at 37% amplitude for 2 min in the ice bath. Then the organic solvent evaporated by continuous stirring overnight. The next day, washing was done three times using ultracentrifuge at 40,000 rpm for 20 min at

Figure 8. *In vivo* anti-tumor or therapeutic efficacy of Nim NPs in nude mice xenograft

(A) Experimental layout for therapeutic studies in tumor-bearing female Balb/c nude mice. Tumor volume and body weight measured twice a week for 51 days, after which the experiment was terminated. (B) Tumor volumes were measured at indicated time points and growth curves of tumors were summarized as mean ± SEM (n = 3 for control and void NPs) and (n = 5 or 6 for Nim or Nim NPs treatment groups), one-way ANOVA with Tukey's multiple comparison test. (C) Image showing tumor excised from mice in different treatment groups at the experimental endpoint. (D) Tumor weight was measured at the end of the experiment. Data represented as mean ± SEM, one-way ANOVA with Tukey's multiple comparison test. (E) The distant metastatic nodes in the liver, lung, and spleen before and after treatment of Nim or Nim NPs in tumor-bearing mice xenograft. (F) The expression of DNMTs, SFRP1, Wnt/β-catenin signaling, and stemness-associated protein markers was examined by immunoblotting in tumors isolated from mice xenograft at the end of the experiment. (G and I) Graphical representation demonstrating the expression of Ki67 and β-catenin in mice tumor tissue respectively by IHC assay. Data represented as mean ± SEM (n = 3), one-way ANOVA with Tukey's multiple comparison test. (H and J) Representative images showing the expression of Ki67 and β-catenin in mice tumor tissues respectively by IHC staining. Scale bar, 20 μm.

4°C (Hitachi Ultracentrifuge CP100NX). After washing, recovered NPs were dispersed in 2 mL of H_2O and sonicated at 37% amplitude for 5 min in the ice bath. Finally, it was lyophilized (LYPHLOCK, Labconco, USA) for 48 h at a temperature of −48°C and pressure of 0.020 mBar. The lyophilized NPs were used for further studies. Void NPs were prepared by the same procedure except that no Nim was added. As the drug is not fluorescent, 6-coumarin NPs were prepared by the same procedure where 100 μg of 6-coumarin was added to the polymeric solution before emulsification loading 0.1% (w/w) of the polymer. The fluorescent 6-coumarin dye incorporated in NPs is a good marker as the dye does not leach from the NPs and has been used in our previous studies to determine the cellular uptake of NPs. IR 780 dye-loaded NPs were prepared similarly, where 5 mg of IR 780 was added to the polymeric solution before emulsification loading 5% (w/w) of the polymer.

Physicochemical characterization of drug-loaded NPs

Particle size measurement

Particle size and polydispersity index of Nim-loaded PLGA NPs were evaluated by dynamic light scattering (DLS) (Zetasizer, Nano ZS, ZEN3600, Malvern Instrument, UK) based on quasi-elastic light scattering. Briefly, ∼1 mg/mL of NPs suspension was prepared in MilliQ water and sonicated using a sonicator (VC 505, Vibracell Sonics, USA) for 30 s at 37% amplitude in an ice bath. The sizes of Nim NPs were measured in triplicates following a 1/100 (v/v) dilution of NPs suspension in MilliQ water at 25°C.

Scanning electron microscope

Nim NPs were evaluated for surface morphology and size by scanning electron microscope (EVO18, Carl Zeiss, Germany) operating at an accelerating voltage of 10–30 kV. For this purpose, a sample of NPs (1 mg/mL) was suspended in water and sonicated using a sonicator (VC 505, Vibracell Sonics, USA) for 20 s at 30% amplitude in an ice bath. Then, 100 μL of this suspension was placed over a coverslip and allowed to dry at 65°C overnight and the images were captured under the microscope.

TEM

The morphology and size of Nim NPs were examined by the TEM 2100 plus electron microscope (JEOL, Tokyo, Japan). A dilute suspension of Nim NPs (1 mg/500 μL dilution) was prepared in double-distilled water and sonicated. One drop of this solution was placed on the TEM grid (01800-F, Ted Pella) for 30 min followed by the NPs stained with 2% uranyl acetate for 3 min then washed twice with double-distilled water and allowed to dry overnight. Images were captured and observed at an accelerating voltage of 120 kV under a microscope as per previously published protocol.[13]

The entrapment efficiency of Nim-loaded NPs

Nim entrapped inside the nanoformulation was estimated by the reverse phase isocratic mode of HPLC using the Waters e2695 consisting of a C18 column, 250 mm × 4.6 mm × 5 μm. Briefly, ∼1 mg of lyophilized Nim-loaded NPs was dissolved in 1 mL of acetonitrile (Spectrochem) and vortexed for 4 min. Then, samples were sonicated at 37% amplitude for 1 min in the ice bath and centrifuged at 13,000 rpm for 10 min at 25°C to extract the drug present in the solution. Then, 1 mL of the supernatant was collected and analyzed using a specific mobile phase; i.e., acetonitrile:water (80:20) ratio. The separation was achieved by isocratic solvent elution at a flow rate of 1 mL/min. Nim level was quantified by UV detection at a wavelength of 207 nm. The amount of Nim in NPs was determined from the peak area correlated with the standard plot prepared under identical conditions. All analysis was performed in triplicates. The entrapment efficiency of Nim used in the formulation was calculated using the following equation: entrapment efficiency (%) = weight of the drug in nanoparticles/weight of drug loaded in the formulation × 100.

Cell line and culture condition

Human TNBC cell line MDA-MB-231 was purchased from American Type Culture Collection (ATCC) (Manassas, VA). Cells were routinely maintained in DMEM media supplemented with 10% fetal bovine serum (PAN-Biotech, Germany) and 1% penicillin-streptomycin (Sigma-Aldrich, St. Louis, USA) at 37°C in a humidified atmosphere of 5% CO_2 (Hera Cell, Thermo Scientific, Waltham, MA).

MDA-MB-231 cells were plated for mammospheres culture at a density of 1×10^5 cells per well in an ultra-low attachment six-well plates (Corning, NY, USA) in stem cell-specific growth medium for a week. The medium from six-well plates was replaced by freshly prepared stem cell growth media on the fourth day. The mammospheres formed on the eighth day were used for experimental purposes. Previously, our lab showed that TNBC adherent cells cultured in stem cell growth media for a week can form mammospheres.[5]

In vitro cellular uptake study

Cellular uptake study was performed by treating mammospheres with 100 ng/mL of native 6-coumarin or 6-coumarin NPs for different points (0.5, 2, 4, and 8 h). At the end of the incubation period, cells were washed with cold PBS and lysed with 100 μL of cell lysis buffer (Sigma-Aldrich, St. Louis, USA) for 30 min. Then cell lysates were lyophilized for 24 h and were reconstituted in 1 mL of acetonitrile and incubated for 2 h in a shaker in the dark. Further, samples were centrifuged once at 14,000 rpm for 10 min at 4°C and the supernatant was collected. The fluorescence intensity of the supernatants was measured by a fluorescence spectrophotometer (PerkinElmer, USA) at an excitation wavelength of 480 nm and an emission wavelength of 525 nm. Qualitative analysis was performed by fluorescence microscopy (Leica, Germany). The differential interference contrast (DIC) and fluorescence images were merged using ImageJ software (NIH, USA).

ALDEFLUOR assay

Aldehyde dehydrogenase (ALDH) enzyme activity in viable cells was determined using a fluorogenic dye-based ALDEFLUOR assay kit as per the manufacturer's instruction. Briefly, mammospheres were cultured as described above and then treated with different concentrations of native Nim and Nim NPs for 48 h. Following treatment, the mammospheres were dissociated enzymatically using accutase. The obtained

single cells were incubated with ALDH substrate for 45 min at 37°C. The samples were incubated under an identical condition in the presence of the ALDH inhibitor diethylaminobenzaldehyde (DEAB), which served as the negative control. The ALDH-positive population following treatment was determined through a flow cytometer (LSR Fortessa, BD Biosciences, CA).

Mammospheres formation assay

For post-treatment assay, primary mammospheres formed after 8 days were treated with different concentrations of native Nim or Nim NPs for 48 h. Following treatment, the number and size of intact mammospheres were determined through the microscope. Mammospheres with a diameter $\geq$ 50 μm were taken into consideration. To assess the residual sphere-forming ability of these treated cells, the cells were enzymatically dissociated using accutase. Then, 5,000 live cells were reseeded in ultra-low attached six-well plates and allowed to grow for an additional 8 days. These cells' sphere-forming ability (secondary spheres) was assessed microscopically by assessing the number and diameter of spheres. Mammospheres with a diameter $\geq$ 50 μm were taken into consideration. For the preventive assay, MDA-MB-231 cells were seeded at a density of 2×10^4 cells/well along with various concentrations of Nim or Nim NPs in stem cell-specific growth medium. After 8 days, the sphere-forming ability of these treated cells was studied through the microscope. Further, the number of mammospheres formed with a diameter $\geq$ 50 μm were counted manually and representative images were acquired using a Leica DM IL LED inverted microscope.

Immunoblotting analysis

MDA-MB-231 cells were plated in six-well plates at a density of 1×10^5 cells per well and grown as mammospheres. Mammospheres were treated with different concentrations of Nim (both native and NPs) for 48 h. After the specified time, total proteins from the above-treated cells or tumor tissues (excised at the end of the experiment) were extracted using radioimmunoprecipitation assay (RIPA) lysis buffer (Sigma-Aldrich, St. Louis, USA) with phosphatase and protease inhibitors. The cell or tissue homogenates were centrifuged at 10,000 rpm for 20 min at 4°C and supernatant was collected. The protein concentration was determined with a Micro BCA Protein Assay Kit (Thermo Fisher Scientific, USA). Whole-cell lysates containing an equal amount of protein were subjected to SDS-polyacrylamide gel electrophoresis and transferred onto polyvinylidene difluoride (PVDF) membrane (GE Healthcare, USA). Membranes were blocked in 5% skim milk powder for 60 min and further incubated with respective primary antibodies (1:1,000 dilutions) overnight at 4°C. Anti-mouse or anti-rabbit horseradish peroxidase-conjugated antibodies were used as secondary antibodies (1:5,000 dilutions) for 45 min at room temperature. The positive signals from the membranes were detected with the reagents in the chemiluminescence detection kit (ECL system; GE Healthcare, USA) according to the manufacturer's instructions. The total intensity of the band for each protein was calculated with ImageJ software (NIH, USA) and normalized with that of β-actin. Primary antibodies used for immunoblotting are listed in Table S2.

Real-time PCR analysis

Mammospheres were treated with different concentrations of Nim and Nim NPs for 48 h. RNA was extracted using TRIzol (Invitrogen) by following the manufacturer's protocol. Total mRNA was reverse transcribed to cDNA using a first-strand cDNA synthesis kit (Thermo Fisher Scientific, USA). cDNA was amplified using GoTaq qPCR Master Mix (Promega) in real-time PCR (QuantStudio 6 Flex Real-Time PCR, Applied Biosciences, USA) using specific primers. Relative quantification of gene expression was executed using the 18S housekeeping gene expression in ΔΔCT. Reactions were performed in triplicate. The primers used in qRT-PCR are listed in Table S3.

Immunofluorescence analysis

Mammospheres were treated with Nim or Nim NPs for 48 h and were plated on a poly-L-lysine (Sigma-Aldrich, USA)-coated coverslip overnight for attachment. The next day, cells were fixed in 4% paraformaldehyde for 15 min at 4°C, permeabilized with 0.1% Triton X-100 (Sigma-Aldrich, St. Louis, USA) for 5 min, followed by blocking with 3% BSA for 1 h at room temperature. Cells were then incubated with the primary antibody overnight at 4°C. Next day, cells were washed thrice with PBS, followed by 1-h incubation with secondary antibody at room temperature. The secondary antibodies used included goat anti-mouse conjugated to FITC (Santa Cruz Biotechnology, sc-2010, 1:1,000), goat anti-rabbit conjugated to Alexa Fluor 647 (Invitrogen, A21244, 2:1,000), and goat anti-rabbit conjugated to Alexa Fluor 488 (Invitrogen, A11008, 1:1,000), respectively. The nuclei of cells were stained with DAPI (Sigma-Aldrich, St. Louis, USA) for 30 min. Cells were again washed thrice with PBS, mounted (Prolong gold antifade, Invitrogen, USA), air-dried, and visualized using a Leica confocal microscope. The primary antibodies used included mouse anti-vimentin (sc-6260, 1:50), rabbit anti-E-cadherin (Cell Signaling Technology, 3195S, 1:100), rabbit anti-DNMT1 (Cell Signaling Technology, 5032S, 1:100), rabbit anti-DNMT3A (Cell Signaling Technology, 3598S, 1:100), and rabbit anti-DNMT3B (Cell Signaling Technology, 57868S, 1:100).

Transwell invasion assay

Cell migration was performed by Transwell assay using 12-well Millicell hanging cell culture inserts (8 μm pore size, Merck Millipore, Billerica, MA). The inserts were coated with 100 μL of 1:1 dilution of DPBS/Matrigel (BD Biosciences) and incubated for 6 h in an incubator at 37°C. Mammospheres were treated with 10 μM Nim or Nim NPs for 48 h in low serum DMEM/F12 medium and added to the upper chamber of the insert. The lower chamber of the Transwell contained stem cell-specific medium. Then, chambers were incubated for 24 h in a CO_2 incubator at 37°C to allow the cells to invade. After incubation, the cells that invaded through the filter toward the lower side were fixed with 4% paraformaldehyde for 20 min at 4°C. The cells were then stained with 0.6% crystal violet for 3 min and the invaded cells were imaged using ZEISS Primostar 3 microscope. The cells in three randomly selected fields were quantified using ImageJ software.

Databases used and bioinformatics analysis

The GEPIA2 database (http://gepia2.cancer-pku.cn) was used to compare the gene expression profile of *SFRP1/2/3/4/5* in breast tumor tissue and normal tissue ($p < 0.05$). The cBioportal database (https://www.cbioportal.org) was used to analyze the correlation between SFRP1 mRNA expression and methylation levels.

DNA isolation, clean-up, and bisulfite modification

After treatment with Nim, Nim NPs, and DAC, mammospheres were lysed and genomic DNA was isolated by use of RNA Biotech (GD-50) kit according to the manufacturer's protocol. Further, the genomic DNA was cleaned up using the Zymo Research (D4065) kit according to the manufacturer's protocol. Genomic DNA was chemically modified by sodium bisulfite to convert all unmethylated cytosines to uracils while leaving methyl cytosines unaltered followed by purification of the bisulfite-converted DNA using the Zymo EZ DNA methylation kit (Zymo Research, D5001) according to the manufacturer's instructions.

MSP assay

For the identification of CpG islands prone to hypermethylation in the SFRP1 sequence, MethPrimer software[64] was used for MSP primer design. To do this, detection criteria were set as default with CpG island size >100 bp, CG percentage >50%, and CpG ratio >60%. Further, the purified and bisulfite-converted DNA was then amplified in a thermocycler using the Taq DNA polymerase and the methylation-specific and unmethylation-specific primers described in Table S4. The following PCR conditions were used: initial denaturation at 95°C for 2 min of one cycle, 35 cycles of 95°C for 30 s, annealing at 55°C for 30 s of 35 cycles, extension at 72°C for 30 s of 35 cycles, and final extension at 72°C for 5 min of one cycle, and the reaction was kept at 4°C until use. After amplification, the MSP products were analyzed by 2% agarose gel electrophoresis. Then, methylation and unmethylation level was quantified through ImageJ software and the relative intensity fold change was evaluated as the ratio of methylated/unmethylated.

ChIP assay

At room temperature, 5×10^6 cells were cross-linked with 1% formaldehyde for 10 min and quenched with 125 mM glycine. ChIP assay was performed by suspending cells in lysis buffer for 15 min on ice and chromatin sonicated using the bioruptor (Bioruptor Pico, Diagenode) for 18 cycles at 4°C. The sheared chromatin was centrifuged at 13,000 rpm for 10 min at 4°C and soluble chromatin was incubated overnight with blocking using 5% BSA followed by 15 μL of magnetic beads (Pierce ChIP-grade Protein A/G Magnetic Beads, Thermo Fisher Scientific, 26162) and 1 μg of antibody against DNMT1 (Thermo Fisher Scientific, PA5120552), and DNMT3A (Thermo Fisher Scientific, PA1882), and immunoglobulin (Ig) G as a negative control (Diagenode, C15410206). Primary antibodies used for ChIP are listed in Table S5. An input fraction corresponding to 1% of starting chromatin was kept for chromatin normalization. Subsequently, beads were separated on a magnetic stand and washed four times on ice with different wash buffers containing different salt concentrations, and bound protein-DNA complexes were eluted from the beads using elution buffer at room temperature. DNA was purified by proteinase K digestion, phenol-chloroform extraction, and ethanol precipitation. The resulting pellet was resuspended in DNA elution buffer (Zymo Research, D3004-4-10). Relative enrichment was measured by ChIP-qPCR. The primers used in ChIP-qPCR are listed in Table S6. ChIP experiments were performed as triplicates. ChIP-qPCR data were normalized by the fold enrichment method (2^{-DDCt}).

Mice xenograft

The Institutional Animal Ethical Review Committee approved all the mice used in the experiment and experimental protocols involved in the animal study (project number ILS/IAEC-128-AH/AUG-18). All of the animals were maintained under pathogen-free conditions in the animal house. For biodistribution, tumorigenicity, and therapeutic studies, 6- to 8-week-old female BALB/c nude mice were used. The orthotopic mice xenograft model was established by injection of 1×10^4 sorted $ALDH^{high}$ BCSCs suspended in 100 μL of PBS and Matrigel (1:1) into the mammary fat pad of nude mice.

In vivo biodistribution study

For *in vivo* biodistribution studies, once the tumor reached 300–400 mm^3 volume, the mice were randomly divided into two groups (n = 3) and each mouse received IR 780 dye intravenously either in native form or in nanoformulation (0.5 mg/kg) dissolved in 100 μL of PBS. The 2D and 3D fluorescence images of the mice were taken at different time points (0.5, 2, 6, and 24 h) post intravenous injection using an *in vivo* imaging system (IVIS Spectrum, PerkinElmer) at an excitation wavelength of 745 nm to collect the signal of IR 780. At 24 h after injection, the mice were sacrificed and the tumor, along with major organs such as the liver, lungs, spleen, kidney, and heart, was isolated and *ex vivo* fluorescent imaging was performed.

In vivo therapeutic study

After the tumor reached ~100 mm^3 in size, the mice were randomly divided into six groups and intravenously administered with a single dose of void NPs, native Nim (10 mg/kg), native Nim (20 mg/kg), Nim NPs (10 mg/kg), Nim NPs (20 mg/kg), and control (treated with only dosing solution) (for control and void NPs n = 3 and for all other groups, n = 6 mice were taken). As mentioned above, all the drug solutions were prepared in a 100-μL dosing solution. The amount of void NPs used was the same as used for Nim NPs (20 mg/kg). Tumor volume and body weight were monitored twice a week for 51 days. Tumor volumes were calculated as follows: $V = (L \times W^2/2)$, where L is the long diameter of the tumor and W is the shortest diameter as measured using a digital Vernier caliper. We kept all treated mice under observation for more than 7 weeks and sacrificed them after 51 days of treatment. At the end of the study, tumor and the major organs such as liver, lungs, spleen, kidney, and heart were isolated, fixed in formalin, and embedded in paraffin for further histological studies through H&E staining and IHC.

IHC

Tumors were isolated, fixed in formalin, and embedded in paraffin wax. Further, tumor tissues were fixed in formalin and embedded in paraffin, and 5-μm-thick sections were cut using a microtome

(Leica RM2125 RTS) and transferred to positively charged slides and allowed to dry overnight. Slides were warmed for 10 min at 65°C before being deparaffinized with xylene, rehydrated in graded ethanol, and hydrated with deionized water subjected to immunohistochemical analysis. Antigen retrieval was done using sodium citrate buffer (Vector Laboratories) at 100°C for 20 min, after which slides were allowed to cool down to room temperature. Inhibition of endogenous peroxidase activity was performed with 3% H_2O_2 (in methanol) for 20 min, followed by blocking with horse serum for 1 h at room temperature. Sections were incubated with primary antibody overnight at 4°C and then incubated with horse anti-rabbit/mouse IgG biotinylated universal secondary antibody (Vector Laboratories, Burlingame, CA) for 1 h at room temperature followed by incubation with ABC reagent for 30 min. To develop stain, 3,3′-diaminobenzidine (DAB; Vector Laboratories) was used as a substrate according to the manufacturer's instructions, and hematoxylin was used as a counter-stain. Sections were dehydrated with ethanol, cleared with xylene, and mounted with VectaMount permanent mounting medium. Sections were observed under the microscope (ZEISS Axio Imager.M2) and images were captured at 40× magnification. Primary antibodies used for IHC, such as Ki67 (ab15580, 1:100) and β-catenin (9562S, 1:100).

Zebrafish xenograft

Zebrafish study was performed by a protocol approved by the Institutional Animal Care and Use Committee (IACUC), ILS (ILS/IAEC-214-AH/APR-21). Embryos were cultured in E3 medium (5 mM NaCl, 0.17 mM KCl, 0.33 mM $CaCl_2$, and 0.33 mM $MgSO_4$) at 28°C. $ALDH^{high}$ BCSCs stained with Dil (Vybrant DiI Cell-Labeling Solution, V22885) for 20 min were transplanted at density of 200 cells/nL, and ∼400 cells were microinjected (Femtojet microinjector) into the perivitelline space of transgenic zebrafish embryos (Danio rerio) (Tg (kdrl: EGFP)) 48 h post fertilization (hpf). Injected embryos were sorted and, 48 h post-injection (hpi), zebrafish were imaged by fluorescence stereomicroscope (Leica MZ16) followed by treatment with either 1 or 2 μM Nim/Nim NPs. At 48 h post treatment (hpt), zebrafish were again imaged to estimate the tumor reduction after treatment. The tumor growth was assessed by an increase or decrease in fluorescence intensity and area at 48 hpt compared to 48 hpi. The quantitation of fluorescence intensity was performed using ImageJ software.

Whole-mount immunofluorescence

Zebrafish xenografts were fixed in 4% formaldehyde overnight and stored in methanol at −20°C. Embryos were washed with 0.1% Triton X-100 in PBS and then blocked for 1 h in PBS with BSA, goat serum, and 10% Triton X-100 at room temperature. Primary antibodies used were anti-DNMT3A (CST, 3598S, 1:100) and anti-β-catenin (CST, 9562S, 1:100), and they were incubated overnight at 4°C and then washed with 0.05% Tween/PBS for 30 min three times. Secondary antibodies Alexa Fluor 488 goat anti-rabbit (1:200) (Invitrogen, A11008) were used and nuclei were counterstained with DAPI diluted in blocking solution. The secondary antibody was removed, washed with 0.05% Tween/PBS, fixed for 20 min in 4% paraformaldehyde, and washed in 0.05% Tween/PBS. After washing, the embryos were mounted in aqueous mounting medium and stored at 4°C. All images were obtained in a fluorescence stereomicroscope (Leica MZ16) and quantification analysis was done with ImageJ software.

Statistical analysis

The mean values of all experiments are given with a standard error of the mean (SEM). The statistical significance of differences was calculated by Student's t test or one-way/two-way ANOVA wherever applicable using GraphPad Prism 9.0.0 software. A p value ≤ 0.05 is considered significant. Significant differences are indicated by *p < 0.05, **p < 0.01, ***p < 0.001, and ****p < 0.0001.

Detailed methods are provided in the supplemental "materials and methods" section.

DATA AND CODE AVAILABILITY

All data generated for this study are included in this published manuscript and relative supplemental information.

SUPPLEMENTAL INFORMATION

Supplemental information can be found online at https://doi.org/10.1016/j.omtn.2023.102031.

ACKNOWLEDGMENTS

This work was supported by core funding from Institute of Life Sciences (Department of Biotechnology, India) to S.K.S. P.M. acknowledges the Department of Science and Technology, Government of India, for an INSPIRE fellowship. We acknowledge Dr. Rupesh Dash for the scientific discussion and overexpression study and Dr. Shantibhusan Senapati for tissue histopathological studies. We acknowledge Neha Singh for helping with MSP primer designing, and Bhabani Sankar Sahoo, Paritosh Nath, Biswajit Patra, Madan Mohan Mallick, and Sushanta Kumar Swain for their technical support. We acknowledge the support of the Institute of Life Sciences central facilities (imaging and FACS), zebrafish facility, and animal house facility funded by the Department of Biotechnology, India.

AUTHOR CONTRIBUTIONS

P.M., conceptualization, methodology, investigation, validation, formal analysis, data curation, writing – original draft, and writing – review & editing; S.M., S.B., P. Singh, and P. Sa, methodology, data curation, and review and editing of the manuscript; P.P. and R.K.S., supervision, validation, review and editing of the manuscript; S.K.S., conceptualization, funding acquisition, supervision, validation, writing – review & editing.

DECLARATION OF INTERESTS

Authors declare no competing interests.

REFERENCES

1. Bianchini, G., De Angelis, C., Licata, L., and Gianni, L. (2022). Treatment landscape of triple-negative breast cancer - expanded options, evolving needs. Nat. Rev. Clin. Oncol. *19*, 91–113. https://doi.org/10.1038/s41571-021-00565-2.

2. Bianchini, G., Balko, J.M., Mayer, I.A., Sanders, M.E., and Gianni, L. (2016). Triple-negative breast cancer: challenges and opportunities of a heterogeneous disease. Nat. Rev. Clin. Oncol. *13*, 674–690. https://doi.org/10.1038/nrclinonc.2016.66.

3. Zheng, Q., Zhang, M., Zhou, F., Zhang, L., and Meng, X. (2020). The Breast Cancer Stem Cells Traits and Drug Resistance. Front. Pharmacol. *11*, 599965. https://doi.org/10.3389/fphar.2020.599965.

4. Singh, P., and Sahoo, S.K. (2022). Piperlongumine loaded PLGA nanoparticles inhibit cancer stem-like cells through modulation of STAT3 in mammosphere model of triple negative breast cancer. Int. J. Pharm. *616*, 121526. https://doi.org/10.1016/j.ijpharm.2022.121526.

5. Singh, D., Singh, P., Pradhan, A., Srivastava, R., and Sahoo, S.K. (2021). Reprogramming Cancer Stem-like Cells with Nanoforskolin Enhances the Efficacy of Paclitaxel in Targeting Breast Cancer. ACS Appl. Bio Mater. *4*, 3670–3685. https://doi.org/10.1021/acsabm.1c00141.

6. Batlle, E., and Clevers, H. (2017). Cancer stem cells revisited. Nat. Med. *23*, 1124–1134. https://doi.org/10.1038/nm.4409.

7. Burnett, J.P., Lim, G., Li, Y., Shah, R.B., Lim, R., Paholak, H.J., McDermott, S.P., Sun, L., Tsume, Y., Bai, S., et al. (2017). Sulforaphane enhances the anticancer activity of taxanes against triple negative breast cancer by killing cancer stem cells. Cancer Lett. *394*, 52–64. https://doi.org/10.1016/j.canlet.2017.02.023.

8. Singh, D., Minz, A.P., and Sahoo, S.K. (2017). Nanomedicine-mediated drug targeting of cancer stem cells. Drug Discov. Today *22*, 952–959. https://doi.org/10.1016/j.drudis.2017.04.005.

9. Mohapatra, P., Singh, P., and Sahoo, S.K. (2020). Phytonanomedicine: a novel avenue to treat recurrent cancer by targeting cancer stem cells. Drug Discov. Today *25*, 1307–1321. https://doi.org/10.1016/j.drudis.2020.06.003.

10. Mohapatra, P., Singh, P., Singh, D., Sahoo, S., and Sahoo, S.K. (2022). Phytochemical based nanomedicine: a panacea for cancer treatment, present status and future prospective. OpenNano *7*, 100055. https://doi.org/10.1016/j.onano.2022.100055.

11. Arumugam, A., Subramani, R., and Lakshmanaswamy, R. (2021). Involvement of actin cytoskeletal modifications in the inhibition of triple-negative breast cancer growth and metastasis by nimbolide. Mol. Ther. Oncolytics *20*, 596–606. https://doi.org/10.1016/j.omto.2021.02.014.

12. Nivetha, R., Arvindh, S., Baba, A.B., Gade, D.R., Gopal, G., C., K., Reddy, K.P., Reddy, G.B., and Nagini, S. (2022). Nimbolide, a Neem Limonoid, Inhibits Angiogenesis in Breast Cancer by Abrogating Aldose Reductase Mediated IGF-1/PI3K/Akt Signalling. Anti Cancer Agents Med. Chem. *22*, 2619–2636. https://doi.org/10.2174/1871520622666220204115151.

13. Singh, D., Mohapatra, P., Kumar, S., Behera, S., Dixit, A., and Sahoo, S.K. (2022). Nimbolide-encapsulated PLGA nanoparticles induces Mesenchymal-to-Epithelial Transition by dual inhibition of AKT and mTOR in pancreatic cancer stem cells. Toxicol. Vitro *79*, 105293. https://doi.org/10.1016/j.tiv.2021.105293.

14. Subramani, R., Gonzalez, E., Arumugam, A., Nandy, S., Gonzalez, V., Medel, J., Camacho, F., Ortega, A., Bonkoungou, S., Narayan, M., et al. (2016). Nimbolide inhibits pancreatic cancer growth and metastasis through ROS-mediated apoptosis and inhibition of epithelial-to-mesenchymal transition. Sci. Rep. *6*, 19819. https://doi.org/10.1038/srep19819.

15. Wu, H.J., and Chu, P.Y. (2021). Epigenetic Regulation of Breast Cancer Stem Cells Contributing to Carcinogenesis and Therapeutic Implications. Int. J. Mol. Sci. *22*, 8113. https://doi.org/10.3390/ijms22158113.

16. Toh, T.B., Lim, J.J., and Chow, E.K.H. (2017). Epigenetics in cancer stem cells. Mol. Cancer *16*, 29. https://doi.org/10.1186/s12943-017-0596-9.

17. Song, K., and Farzaneh, M. (2021). Signaling pathways governing breast cancer stem cells behavior. Stem Cell Res. Ther. *12*, 245. https://doi.org/10.1186/s13287-021-02321-w.

18. Jang, G.B., Kim, J.Y., Cho, S.D., Park, K.S., Jung, J.Y., Lee, H.Y., Hong, I.S., and Nam, J.S. (2015). Blockade of Wnt/β-catenin signaling suppresses breast cancer metastasis by inhibiting CSC-like phenotype. Sci. Rep. *5*, 12465. https://doi.org/10.1038/srep12465.

19. Veeck, J., Niederacher, D., An, H., Klopocki, E., Wiesmann, F., Betz, B., Galm, O., Camara, O., Dürst, M., Kristiansen, G., et al. (2006). Aberrant methylation of the Wnt antagonist SFRP1 in breast cancer is associated with unfavourable prognosis. Oncogene *25*, 3479–3488. https://doi.org/10.1038/sj.onc.1209386.

20. Cheng, Z., Yu, R., Li, L., Mu, J., Gong, Y., Wu, F., Liu, Y., Zhou, X., Zeng, X., Wu, Y., et al. (2022). Disruption of ZNF334 promotes triple-negative breast carcinoma malignancy through the SFRP1/Wnt/β-catenin signaling axis. Cell. Mol. Life Sci. *79*, 280. https://doi.org/10.1007/s00018-022-04295-1.

21. Lo, P.K., Mehrotra, J., D'Costa, A., Fackler, M.J., Garrett-Mayer, E., Argani, P., and Sukumar, S. (2006). Epigenetic suppression of secreted frizzled related protein 1 (SFRP1) expression in human breast cancer. Cancer Biol. Ther. *5*, 281–286. https://doi.org/10.4161/cbt.5.3.2384.

22. Pop, S., Enciu, A.M., Tarcomnicu, I., Gille, E., and Tanase, C. (2019). Phytochemicals in cancer prevention: modulating epigenetic alterations of DNA methylation. Phytochem. Rev. *18*, 1005–1024. https://doi.org/10.1007/s11101-019-09627-x.

23. Carlos-Reyes, Á., López-González, J.S., Meneses-Flores, M., Gallardo-Rincón, D., Ruíz-García, E., Marchat, L.A., Astudillo-de la Vega, H., Hernández de la Cruz, O.N., and López-Camarillo, C. (2019). Dietary Compounds as Epigenetic Modulating Agents in Cancer. Front. Genet. *10*, 79. https://doi.org/10.3389/fgene.2019.00079.

24. Shankar, S., Kumar, D., and Srivastava, R.K. (2013). Epigenetic modifications by dietary phytochemicals: implications for personalized nutrition. Pharmacol. Ther. *138*, 1–17. https://doi.org/10.1016/j.pharmthera.2012.11.002.

25. Shi, J., Kantoff, P.W., Wooster, R., and Farokhzad, O.C. (2017). Cancer nanomedicine: progress, challenges and opportunities. Nat. Rev. Cancer *17*, 20–37. https://doi.org/10.1038/nrc.2016.108.

26. Sahoo, S.K., and Labhasetwar, V. (2005). Enhanced antiproliferative activity of transferrin-conjugated paclitaxel-loaded nanoparticles is mediated via sustained intracellular drug retention. Mol. Pharm. *2*, 373–383. https://doi.org/10.1021/mp050032z.

27. Arya, G., Das, M., and Sahoo, S.K. (2018). Evaluation of curcumin loaded chitosan/PEG blended PLGA nanoparticles for effective treatment of pancreatic cancer. Biomed. Pharmacother. *102*, 555–566. https://doi.org/10.1016/j.biopha.2018.03.101.

28. Rivolta, I., Panariti, A., Lettiero, B., Sesana, S., Gasco, P., Gasco, M.R., Masserini, M., and Miserocchi, G. (2011). Cellular uptake of coumarin-6 as a model drug loaded in solid lipid nanoparticles. J. Physiol. Pharmacol. *62*, 45–53.

29. Shi, X., Zhang, Y., Zheng, J., and Pan, J. (2012). Reactive oxygen species in cancer stem cells. Antioxid. Redox Signal. *16*, 1215–1228. https://doi.org/10.1089/ars.2012.4529.

30. Skvortsova, I., Debbage, P., Kumar, V., and Skvortsov, S. (2015). Radiation resistance: Cancer stem cells (CSCs) and their enigmatic pro-survival signaling. Semin. Cancer Biol. *35*, 39–44. https://doi.org/10.1016/j.semcancer.2015.09.009.

31. Wang, K., Zhang, T., Dong, Q., Nice, E.C., Huang, C., and Wei, Y. (2013). Redox homeostasis: the linchpin in stem cell self-renewal and differentiation. Cell Death Dis. *4*, e537. https://doi.org/10.1038/cddis.2013.50.

32. Liu, J.F., Hou, C.H., Lin, F.L., Tsao, Y.T., and Hou, S.M. (2015). Nimbolide Induces ROS-Regulated Apoptosis and Inhibits Cell Migration in Osteosarcoma. Int. J. Mol. Sci. *16*, 23405–23424. https://doi.org/10.3390/ijms161023405.

33. Shan, N.L., Shin, Y., Yang, G., Furmanski, P., and Suh, N. (2021). Breast cancer stem cells: A review of their characteristics and the agents that affect them. Mol. Carcinog. *60*, 73–100. https://doi.org/10.1002/mc.23277.

34. Das, S., Mukherjee, P., Chatterjee, R., Jamal, Z., and Chatterji, U. (2019). Enhancing Chemosensitivity of Breast Cancer Stem Cells by Downregulating SOX2 and ABCG2 Using Wedelolactone-encapsulated Nanoparticles. Mol. Cancer Ther. *18*, 680–692. https://doi.org/10.1158/1535-7163.Mct-18-0409.

35. Brabletz, T. (2012). EMT and MET in metastasis: where are the cancer stem cells? Cancer Cell *22*, 699–701. https://doi.org/10.1016/j.ccr.2012.11.009.

36. Wang, Z., Wang, N., Li, W., Liu, P., Chen, Q., Situ, H., Zhong, S., Guo, L., Lin, Y., Shen, J., and Chen, J. (2014). Caveolin-1 mediates chemoresistance in breast cancer stem cells via β-catenin/ABCG2 signaling pathway. Carcinogenesis *35*, 2346–2356. https://doi.org/10.1093/carcin/bgu155.

37. Suzuki, H., Toyota, M., Carraway, H., Gabrielson, E., Ohmura, T., Fujikane, T., Nishikawa, N., Sogabe, Y., Nojima, M., Sonoda, T., et al. (2008). Frequent epigenetic inactivation of Wnt antagonist genes in breast cancer. Br. J. Cancer *98*, 1147–1156. https://doi.org/10.1038/sj.bjc.6604259.

38. Liang, C.J., Wang, Z.W., Chang, Y.W., Lee, K.C., Lin, W.H., and Lee, J.L. (2019). SFRPs Are Biphasic Modulators of Wnt-Signaling-Elicited Cancer Stem Cell

Properties beyond Extracellular Control. Cell Rep. *28*, 1511–1525.e5. https://doi.org/10.1016/j.celrep.2019.07.023.

39. Suriano, G., Vrcelj, N., Senz, J., Ferreira, P., Masoudi, H., Cox, K., Nabais, S., Lopes, C., Machado, J.C., Seruca, R., et al. (2005). beta-catenin (CTNNB1) gene amplification: a new mechanism of protein overexpression in cancer. Genes Chromosomes Cancer *42*, 238–246. https://doi.org/10.1002/gcc.20135.

40. Hegde, M., and Joshi, M.B. (2021). Comprehensive analysis of regulation of DNA methyltransferase isoforms in human breast tumors. J. Cancer Res. Clin. Oncol. *147*, 937–971. https://doi.org/10.1007/s00432-021-03519-4.

41. Maeda, H., Wu, J., Sawa, T., Matsumura, Y., and Hori, K. (2000). Tumor vascular permeability and the EPR effect in macromolecular therapeutics: a review. J. Control. Release *65*, 271–284. https://doi.org/10.1016/s0168-3659(99)00248-5.

42. Acharya, S., and Sahoo, S.K. (2011). PLGA nanoparticles containing various anticancer agents and tumour delivery by EPR effect. Adv. Drug Deliv. Rev. *63*, 170–183. https://doi.org/10.1016/j.addr.2010.10.008.

43. Mori, Y., Yamawaki, K., Ishiguro, T., Yoshihara, K., Ueda, H., Sato, A., Ohata, H., Yoshida, Y., Minamino, T., Okamoto, K., and Enomoto, T. (2019). ALDH-Dependent Glycolytic Activation Mediates Stemness and Paclitaxel Resistance in Patient-Derived Spheroid Models of Uterine Endometrial Cancer. Stem Cell Rep. *13*, 730–746. https://doi.org/10.1016/j.stemcr.2019.08.015.

44. Park, M., Kim, D., Ko, S., Kim, A., Mo, K., and Yoon, H. (2022). Breast Cancer Metastasis: Mechanisms and Therapeutic Implications. Int. J. Mol. Sci. *23*, 6806. https://doi.org/10.3390/ijms23126806.

45. Shima, H., Yamada, A., Ishikawa, T., and Endo, I. (2017). Are breast cancer stem cells the key to resolving clinical issues in breast cancer therapy? Gland Surg. *6*, 82–88. https://doi.org/10.21037/gs.2016.08.03.

46. Saeg, F., and Anbalagan, M. (2018). Breast cancer stem cells and the challenges of eradication: a review of novel therapies. Stem Cell Investig. *5*, 39. https://doi.org/10.21037/sci.2018.10.05.

47. Nalla, L.V., Kalia, K., and Khairnar, A. (2019). Self-renewal signaling pathways in breast cancer stem cells. Int. J. Biochem. Cell Biol. *107*, 140–153. https://doi.org/10.1016/j.biocel.2018.12.017.

48. Zhan, T., Rindtorff, N., and Boutros, M. (2017). Wnt signaling in cancer. Oncogene *36*, 1461–1473. https://doi.org/10.1038/onc.2016.304.

49. Sahoo, S.K., Parveen, S., and Panda, J.J. (2007). The present and future of nanotechnology in human health care. Nanomedicine. *3*, 20–31. https://doi.org/10.1016/j.nano.2006.11.008.

50. Dilnawaz, F., Acharya, S., and Sahoo, S.K. (2018). Recent trends of nanomedicinal approaches in clinics. Int. J. Pharm. *538*, 263–278. https://doi.org/10.1016/j.ijpharm.2018.01.016.

51. Panyam, J., Sahoo, S.K., Prabha, S., Bargar, T., and Labhasetwar, V. (2003). Fluorescence and electron microscopy probes for cellular and tissue uptake of poly(D,L-lactide-co-glycolide) nanoparticles. Int. J. Pharm. *262*, 1–11. https://doi.org/10.1016/s0378-5173(03)00295-3.

52. Diehn, M., Cho, R.W., Lobo, N.A., Kalisky, T., Dorie, M.J., Kulp, A.N., Qian, D., Lam, J.S., Ailles, L.E., Wong, M., et al. (2009). Association of reactive oxygen species levels and radioresistance in cancer stem cells. Nature *458*, 780–783. https://doi.org/10.1038/nature07733.

53. Ryoo, I.G., Choi, B.H., Ku, S.K., and Kwak, M.K. (2018). High CD44 expression mediates p62-associated NFE2L2/NRF2 activation in breast cancer stem cell-like cells: Implications for cancer stem cell resistance. Redox Biol. *17*, 246–258. https://doi.org/10.1016/j.redox.2018.04.015.

54. Kahroba, H., Shirmohamadi, M., Hejazi, M.S., and Samadi, N. (2019). The Role of Nrf2 signaling in cancer stem cells: From stemness and self-renewal to tumorigenesis and chemoresistance. Life Sci. *239*, 116986. https://doi.org/10.1016/j.lfs.2019.116986.

55. Wu, T., Harder, B.G., Wong, P.K., Lang, J.E., and Zhang, D.D. (2015). Oxidative stress, mammospheres and Nrf2-new implication for breast cancer therapy? Mol. Carcinog. *54*, 1494–1502. https://doi.org/10.1002/mc.22202.

56. Liu, X., and Fan, D. (2015). The epithelial-mesenchymal transition and cancer stem cells: functional and mechanistic links. Curr. Pharm. Des. *21*, 1279–1291. https://doi.org/10.2174/1381612821666141211115611.

57. Shibue, T., and Weinberg, R.A. (2017). EMT, CSCs, and drug resistance: the mechanistic link and clinical implications. Nat. Rev. Clin. Oncol. *14*, 611–629. https://doi.org/10.1038/nrclinonc.2017.44.

58. Xie, Q., Chen, L., Shan, X., Shan, X., Tang, J., Zhou, F., Chen, Q., Quan, H., Nie, D., Zhang, W., et al. (2014). Epigenetic silencing of SFRP1 and SFRP5 by hepatitis B virus X protein enhances hepatoma cell tumorigenicity through Wnt signaling pathway. Int. J. Cancer *135*, 635–646. https://doi.org/10.1002/ijc.28697.

59. Baira, S.M., Khurana, A., Somagoni, J., Srinivas, R., Godugu, C., and Talluri, M.V.N.K. (2018). First report on the pharmacokinetic profile of nimbolide, a novel anticancer agent in oral and intravenous administrated rats by LC/MS method. J. Chromatogr. B Analyt. Technol. Biomed. Life Sci. *1092*, 191–198. https://doi.org/10.1016/j.jchromb.2018.06.002.

60. Hason, M., and Bartůněk, P. (2019). Zebrafish Models of Cancer-New Insights on Modeling Human Cancer in a Non-Mammalian Vertebrate. Genes *10*, 935. https://doi.org/10.3390/genes10110935.

61. Cui, J.H., Krueger, U., Henne-Bruns, D., Kremer, B., and Kalthoff, H. (2001). Orthotopic transplantation model of human gastrointestinal cancer and detection of micrometastases. World J. Gastroenterol. *7*, 381–386. https://doi.org/10.3748/wjg.v7.i3.381.

62. Nakayama, J., Han, Y., Kuroiwa, Y., Azuma, K., Yamamoto, Y., and Semba, K. (2021). The In Vivo Selection Method in Breast Cancer Metastasis. Int. J. Mol. Sci. *22*, 1886. https://doi.org/10.3390/ijms22041886.

63. Bailey-Downs, L.C., Thorpe, J.E., Disch, B.C., Bastian, A., Hauser, P.J., Farasyn, T., Berry, W.L., Hurst, R.E., and Ihnat, M.A. (2014). Development and characterization of a preclinical model of breast cancer lung micrometastatic to macrometastatic progression. PLoS One *9*, e98624. https://doi.org/10.1371/journal.pone.0098624.

64. Li, L.C., and Dahiya, R. (2002). MethPrimer: designing primers for methylation PCRs. Bioinformatics *18*, 1427–1431. https://doi.org/10.1093/bioinformatics/18.11.1427.